

LA-UR-14-25308 (Accepted Manuscript)

Effect of spatial density variation and O⁺ concentration on the growth and evolution of electromagnetic ion cyclotron waves

Denton, R. E.
Jordanova, Vania Koleva
Fraser, B. J.

Provided by the author(s) and the Los Alamos National Laboratory (2016-10-13).

To be published in: Journal of Geophysical Research: Space Physics

DOI to publisher's version: 10.1002/2014JA020384

Permalink to record: <http://permalink.lanl.gov/object/view?what=info:lanl-repo/lareport/LA-UR-14-25308>

Disclaimer:

Approved for public release. Los Alamos National Laboratory, an affirmative action/equal opportunity employer, is operated by the Los Alamos National Security, LLC for the National Nuclear Security Administration of the U.S. Department of Energy under contract DE-AC52-06NA25396. Los Alamos National Laboratory strongly supports academic freedom and a researcher's right to publish; as an institution, however, the Laboratory does not endorse the viewpoint of a publication or guarantee its technical correctness.

1 Effect of Spatial Density Variation and O+
2 Concentration on the Growth and Evolution of
3 Electromagnetic Ion Cyclotron Waves

R. E. Denton,¹ V. K. Jordanova,² B. J. Fraser,³

R. E. Denton, Department of Physics and Astronomy, Dartmouth College, Hanover, NH 03755, USA. (richard.e.denton@dartmouth.edu)

B. J. Fraser, Center for Space Physics, University of Newcastle, Callaghan, New South Wales, Australia. (brian.fraser@newcastle.edu.au)

V. K. Jordanova, Los Alamos National Lab, MS D466, Los Alamos, NM 87545-0000, USA. (vania@lanl.gov)

¹Department of Physics and Astronomy,
Dartmouth College, Hanover, New
Hampshire, USA

²Los Alamos National Lab, Los Alamos,
New Mexico, USA

³Center for Space Physics, University of
Newcastle, Callaghan, New South Wales,
Australia

Abstract. We simulate electromagnetic ion cyclotron (EMIC) wave growth and evolution within three regions, the plasmasphere (or plasmaspheric plume), the plasmopause, and the low density plasmatrough outside the plasmopause. First we use a ring current simulation with a plasmasphere model to model the particle populations that give rise to the instability for conditions observed on 9 June, 2001. Then, using two different models for the cold ion composition, we do a full scale hybrid code simulation in dipole coordinates of the EMIC waves on a meridional plane at MLT = 18 and at 1900 UT within a range of L shell from $L = 4.9$ to 6.7. EMIC waves were observed during June 9, 2001 by Geostationary Operational Environmental Satellite (GOES) spacecraft. While an exact comparison between observed and simulated spectra is not possible here, we do find significant similarities between the two, at least at one location within the region of largest wave growth. We find that the plasmopause is not a preferred region for EMIC wave growth, though waves can grow in that region. The density gradient within the plasmopause does, however, affect the orientation of wave fronts and wave vector both within the plasmopause and in adjacent regions. There is a preference for EMIC waves to be driven in the He+ band (frequencies between the O+ and He+ gyrofrequencies) within the plasmasphere, although they can also grow in the plasmatrough. If present, H+ band waves are more likely to grow in the plasmatrough. This fact, plus L dependence of the frequency and possible time evolution toward lower frequency waves can be explained by a simple model. Large O+ concentration limits the frequency range of or even totally quenches

27 EMIC waves. This is more likely to occur in the plasmatrough at solar max-
28 imum. Such large O⁺ concentration significantly affects the H⁺ cutoff fre-
29 quency, and hence the width in frequency of the stop band above the He⁺
30 gyrofrequency. EMIC wave surfaces predicted by cold plasma theory are al-
31 tered by the finite temperature of the ring current H⁺.

1. Introduction

Electromagnetic ion cyclotron (EMIC) waves are currently thought to be an important loss mechanism for radiation belt electrons [Meredith *et al.*, 2003; Shprits *et al.*, 2008; Millan and Thorne, 2007]. Losses occur through pitch angle scattering into the loss cone [Millan and Thorne, 2007; Jordanova *et al.*, 2008] and may empty the entire radiation belts over a timescale of a few hours [Selesnick, 2006]. EMIC waves may tend to regulate the proton ring current (energy ~ 1 to 100 keV) temperature ratio T_{\perp}/T_{\parallel} , where T_{\perp} and T_{\parallel} are the temperatures relatively perpendicular or parallel to the background magnetic field [Blum *et al.*, 2009], and may also cause precipitation of ring current protons [Jordanova *et al.*, 2001a; Yahnina *et al.*, 2003]. Therefore, EMIC waves have significant effects on energetic particle populations, and it is important to understand the evolution and properties of these waves.

Considering a plasma consisting of H+, He+, and O+ ions, EMIC waves can occur in three wave bands [Andre, 1985; Hu *et al.*, 2010]. Each of these has a frequency that approaches the gyrofrequency of a particular ion for waves propagating roughly parallel to the background magnetic field ($k_{\parallel} \gg k_{\perp}$) at large parallel component of the wave vector k_{\parallel} , and each wave band is named for that ion. Thus the H+ band, He+ band, and O+ band waves asymptote respectively to the H+ gyrofrequency, the He+ gyrofrequency, and the O+ gyrofrequency at large k_{\parallel} .

The unstable region of each wave dispersion surface is in the left hand polarized part of the surface where the frequency has a significant slope with respect to k_{\parallel} and is not too close to the gyrofrequency of the ion corresponding to the named band (He+ for the

He+ band). Very close to the gyrofrequency, there is so-called “cyclotron damping”. For nearly parallel propagation ($k_{\perp} \ll k_{\parallel}$), the O+ band continues to be left hand polarized as the frequency is reduced, but as the frequency is reduced on the H+ and He+ bands there may be different behavior. For a cold plasma and at finite wave normal angle θ_{kB} between the wave vector \mathbf{k} and the magnetic field \mathbf{B} , there is a crossover frequency at which the polarization becomes right hand polarized. There is also a left hand polarized surface at frequencies below the crossover frequency, but for a cold plasma at finite θ_{kB} this surface connects topologically to the higher frequency mode (to the whistler mode within the H+ band and to the H+ band within the He+ band) [Andre, 1985; Hu et al., 2010]. There are cutoff frequencies for both of these surfaces. The cutoff frequencies within the He+ band are above the O+ gyrofrequency. For all these surfaces, as k_{\perp} becomes comparable to k_{\parallel} , the polarization shifts toward linear polarization.

EMIC waves are usually most unstable in the vicinity of the magnetic equator where the anisotropy and plasma beta are largest [Hu and Denton, 2009; Hu et al., 2010]. The group velocity of EMIC waves is approximately along the magnetic field, so EMIC wave energy propagates along the magnetic field away from the magnetic equator toward the ionosphere. As the waves propagate toward the ionosphere, the wave frequency remains constant, but the gyrofrequencies of the various ion species increase due to the increasing magnetic field. Because of this, the wave frequency normalized to the gyrofrequency decreases. Often the wave vector turns significantly oblique at large latitudes, so that the polarization becomes linear [Hu and Denton, 2009; Hu et al., 2010]. But the waves might refract less strongly. Then as the waves propagate toward the ionosphere, if the cold

plasma dispersion surfaces are applicable, the polarization would change from left handed to right-handed (after passing through the crossover frequency), and then to linear.

Various approaches have been used to study the evolution and growth of these waves. *Gary et al.* [1994a] and *Blum et al.* [2009] used local linear kinetic theory and one dimensional hybrid code simulations to derive final states resulting from EMIC waves. *Jordanova et al.* [2001a, 2008] used a kinetic ring current model to calculate the equatorial growth rate of EMIC waves during storm time and found maximum values in the postnoon-to-midnight MLT sector where the intense anisotropic ring current overlapped with the plasmaspheric bulge and drainage plumes.

Chen et al. [2010], following *Horne and Thorne* [1997, and references therein] calculated EMIC wave growth using a ray tracing code and found that EMIC waves occurred in the high density plume, especially on the eastward side of a plume extending somewhat outward radially, and just inside the plasmopause. *Gamayunov and Khazanov* [2008] and *Gamayunov et al.* [2009] used a bounce averaged wave equation to examine the inner magnetospheric system with coupled ring current population and EMIC waves. *Gamayunov and Khazanov* [2008] found that medium energy (~ 1 keV) protons from the plasmasheet in the dawn local time sector can significantly modify the real part of the wave dispersion. *Gamayunov et al.* [2009] found significant variation in results depending on the ionospheric model.

Omidi et al. [2010] used a two dimensional hybrid code to find that the saturation mechanism of the waves involved gyrophase bunching and growth of electrostatic waves. *Bortnik et al.* [2011] used two dimensional hybrid code simulations to find a formula relating the saturation amplitude to the linear growth rate. *Shoji and Omura* [2011] and

Shoji et al. [2011] used one dimensional hybrid code simulations with inhomogeneity along the magnetic field to show that EMIC waves could be triggered by other emissions; they were able to simulate EMIC waves with “rising tone” frequency.

Omidi et al. [2011, 2013] used a two dimensional hybrid code simulation with a line dipole to simulate EMIC waves in a plane with inhomogeneity similar to that of a dipole magnetic field. *Omidi et al.* [2011] showed that injected ring current ions lead to a reduction in total density and magnetic field, in part because of the waves. *Omidi et al.* [2013] found that the character of the waves depended strongly on the cold O+ concentration [similar to, though not exactly the same, as results by *Hu et al.*, 2010]. They also showed that the waves were heavily damped when the O+ concentration was large.

Here we will do hybrid code (particle ions and inertialess electron fluid) simulations of EMIC waves using the same simulation code that was used by *Hu and Denton* [2009] and *Hu et al.* [2010]. These simulations are performed in a dipole geometry with a limited range of L shell, and using a particle population initialized with an anisotropic MHD equilibrium. These features allow for a high resolution low noise simulation. *Hu and Denton* [2009] found that the waves are coherent over a limited range in L . *Hu et al.* [2010] found that the character of the waves changed as the concentration of cold O+ ions increased. At high O+ concentration, the wave power was lower, and the waves were confined within a smaller range of magnetic latitude MLAT. These observations will be relevant for the current study.

A major focus of this paper will be on the effects of a plasmopause on the waves. While we call this negative gradient with respect to L a plasmopause, it could just as well be the radially outer part of a plasmaspheric plume. We simulate the wave growth and

evolution within the plasmopause itself and on both sides of the plasmopause, within the high density plasmasphere and the low density plasmatrough.

Observational surveys by *Anderson et al.* [1992a] and *Fraser and Nguyen* [2001] did not show a preference for waves within the plasmasphere, but some recent studies of EMIC waves have shown a preference for occurrence within a plasmaspheric plume [*Spasojevic et al.*, 2004; *Yahnin and Yahnina*, 2007]. *Usanova et al.* [2013] found using data from the Cluster spacecraft that the probability of EMIC waves inside a plume was significantly higher than that outside, especially immediately outside. But they did not find that high density within the plume increased the probability of EMIC waves. They did find that the waves were most correlated with high dynamic pressure, which can lead to higher temperature anisotropy [*Anderson and Hamilton*, 1993].

Halford et al. [2014], using data from the Combined Release and Radiation Effects Satellite (CRRES), found that on average when EMIC waves are observed, the plasma density is significantly higher than when EMIC waves are not observed. *Chen et al.* [2009] and *Chen et al.* [2010] suggest that guiding of waves by an inward density gradient is an important factor determining wave growth, but Halford et al. found that there was no correlation between occurrence of EMIC waves and a negative density gradient.

We will be simulating EMIC waves using parameters from the Ring current-Atmosphere interactions Model with Self-Consistent magnetic field (B), RAM-SCB [*Jordanova et al.*, 2006, 2012; *Chen et al.*, 2010]. That simulation code was used to model the ring current and cold density populations on June 9, 2001, during which a geomagnetic storm occurred, and the wave growth of EMIC waves for this event was modeled by *Chen et al.* [2014]. Examining the wave growth at several times, they found that the waves grew most strongly

during the main phase of the storm at UT = 1900 at or near the outer boundary of their simulation at $L = 6.5$.

Here we will model the waves at 1900 UT within a range of L shell from 4.9 to 6.7. Whereas the calculations of *Chen et al.* [2014] find the EMIC wave growth in the equatorial plane (assuming growth predominantly within 10° of the magnetic equator), our simulation will be on a meridional plane at a single value of MLT = 18 (dusk local time). Our simulation is complementary in that it yields a more detailed description of the wave growth within a narrow range of L and along the magnetic field lines.

In Section 2 we briefly describe the RAM-SCB and hybrid simulation codes; in Section 3, we describe results from the RAM-SCB simulation; in Section 4 we describe the hybrid code results using the RAM-SCB results as input; and in Section 5 we discuss and summarize our results.

2. Simulation Codes

2.1. Description of RAM-SCB Simulation Code

The RAM-SCB code simulates the dynamics of the ring current that provides free energy for the EMIC waves. RAM-SCB couples two codes. The first of these is the Ring current-Atmosphere interactions Model (RAM), which solves the bounce-averaged kinetic equation for the major ring current species [*Jordanova et al.*, 2012, and references therein]. The second is a 3-D Euler-potential-based plasma equilibrium code [*Zaharia et al.*, 2010, and references therein] which solves for the magnetic field assuming a state of force balance with the plasma pressure provided from RAM. RAM solves for the bounce-averaged distribution function for H+, He+, and O+ ring current ions versus magnetic local time (MLT) and L shell varying from 2 to 6.5.

The inner and outer magnetic flux surface of SCB is obtained by field-line tracing using the empirical magnetic field model of *Tsyganenko and Sitnov* [2005]. To calculate the electric field drift velocities, the empirical convection electric field model of *Weimer* [2001] (W01) is added to the time-independent co-rotation electric field. The W01 ionospheric potential is driven by time-dependent inter-planetary data; and the AL index is mapped to the Solar Magnetic (SM) equatorial plane along the SCB field lines. The RAM model also includes loss processes for ring current ions, including charge-exchange with geocoronal hydrogen, Coulomb collisions with thermal plasma, and loss due to collisions with the dense atmosphere at low altitudes [for more details, see *Jordanova et al.*, 1996, 2001a]. The RAM model also includes the time-dependent plasmasphere model of *Rasmussen et al.* [1993], which calculates the ExB drift motion of individual flux tubes and includes supply and loss rates.

To set the initial conditions for the RAM model, we use differential ion fluxes measured with the the HYDRA (H⁺ at energies <20 keV) and MICS (H⁺, He⁺ and O⁺ at energies >1 keV) instruments on the Polar satellite during a quiet time period [*Jordanova et al.*, 2001b, and references therein], and run the model for more than 10 hours of quiet time before storm commencement to establish prestorm conditions characteristic for the investigated period. The nightside boundary conditions for the ring current ions are determined from plasma sheet flux measurements from the Magnetospheric Plasma Analyzer (MPA) and Synchronous Orbit Particle Analyzers (SOPA) instruments on the LANL geosynchronous spacecraft. The MLT dependence of the data for the nightside boundary is preserved and the dependence of the ion composition with geomagnetic and solar activity is adopted using the study of *Young et al.* [1982].

We note that wave-particle interactions are not included in this study so there is no plasma wave scattering feedback on the particle distributions. This means that the ring current particle populations are in a more unstable state than would be allowed if the ring current populations and EMIC waves were evolved self consistently. And consequently, the wave growth would likely be smaller using a self consistent ring current simulation.

2.2. Description of Hybrid Code

The hybrid code was described in detail by *Hu and Denton* [2009] and *Hu et al.* [2010]. Particles are used for the ions, while the electrons are described by an inertialess fluid. The plasma is quasi-neutral, so the electron density is equal to the ion density. The magnetic field is advanced using Faraday's law. The electric field is found from $\mathbf{E} = -\mathbf{u}_e \times \mathbf{B} + \eta \mathbf{J}$, where \mathbf{B} is the magnetic field, $\mathbf{J} = \nabla \times \mathbf{B}$ (Ampere's law) and \mathbf{u}_e is the electron velocity found using $\mathbf{J} = \mathbf{J}_i - en_e \mathbf{u}_e$ where \mathbf{J}_i is the ion density and n_e is the electron density. The resistivity η is nonzero only near the boundaries, where it damps the waves [*Hu and Denton*, 2009]. Other than at these boundary regions, the parallel electric field is zero. Therefore one limitation of our simulation is that there is no electron Landau damping. Landau damping would cause a reduction in obliquely propagating waves, that is, waves with wave vector not parallel to \mathbf{B} , in the later parts of the simulation.

The hybrid code uses generalized orthogonal coordinates [*Arfken*, 1970], and here we employ dipole coordinates. This doesn't mean that the equilibrium magnetic field is dipolar. The initial magnetic field is found from an anisotropic MHD simulation [*Hu et al.*, 2010] so that the initial plasma configuration is in MHD equilibrium. This results in a low noise simulation in which the subsequent evolution is due entirely to the evolution and effects of the EMIC waves.

The simulations are two dimensional representing a meridional plane. Only the northern half of this plane is simulated; symmetry conditions are used at the magnetic equator. The first coordinate q varies along the dipole magnetic field with value 0 at the magnetic equator and a value of 1 at our ionospheric boundary that is at a magnetic latitude MLAT of 47° for the central L shell in the simulation. This range of latitude is large enough that the waves have passed through all relevant resonant surfaces before they reach the ionospheric boundary where they are damped. The q coordinate is chosen so that equal spacing in q corresponds to a distance in real space proportional to B at the central L shell in the simulation. (Since the coordinates are orthogonal, surfaces of constant q are also surfaces of the usual dipole coordinate that is orthogonal to L . There is freedom to choose a particular mapping between q and distance only at one particular L shell.) Since flux tubes have area $\propto 1/B$, the volume of each cell in the simulation is exactly constant along the central field line and roughly constant at other L values; this is a good choice for simulation of Alfvén waves, and leads to an even distribution of particles, which is good for keeping the numerical noise low. The second coordinate in our simulation is the dipole L value, which in this case varies from 4.9 to 6.7.

The simulations here are full scale. We used 401 grid points along the dipole magnetic field and 301 across the magnetic field (across L shell) with grid points on the boundaries. These values were chosen in order to well resolve the relevant spatial scales, and the resolution of these simulations is higher than those of previous two dimensional simulations [e.g. *Hu et al.*, 2010]. There are about 25 grid points per dominant parallel wavelength at the magnetic equator, and these waves are also resolved at higher latitude. At the central L shell, there were about 4 grid points per thermal gyroradius of the ring current protons,

so the wave structure is well resolved on this scale. The simulation we describe here includes a plasmopause, and there are 83 grid points across the plasmopause, so it also is well resolved. There were 768 particles per grid point used to simulate the ring current H+ and 448 particles per grid point used to simulate the ring current O+; 64 particles per grid point were used to simulate each of the four remaining particle populations, ring current He+, cold H+, cold He+, and cold O+.

3. RAM-SCB Simulation Results

Figure 1 shows quantities from the RAM-SCB simulation, with the particular goal of showing where EMIC waves are likely to be most unstable based on the local parameters. The pressure of the ring current O+ in the simulation yields a fairly large plasma beta ($\beta = P/(B^2/(2\mu_0))$) and anisotropy ($A = P_{\perp}/P_{\parallel} - 1$) by itself, which suggests that it might lead to instability in the O+ frequency band (with an upper limit of Ω_{cO}); we do not find, however, any growth in this band in our hybrid code simulation results. *Chen et al.* [2014] also did not predict any wave growth in the O+ band based on their linear growth calculations using ray tracing. The plasma beta of the He+ population was low. Therefore we concentrate here on the instability driven by the H+ population. Here, P is the plasma pressure, P_{\parallel} and P_{\perp} are the plasma pressure components respectively parallel and perpendicular to the magnetic field, B is the magnetic field, and μ_0 is the magnetic permeability.

Figure 1a shows the plasma beta $\beta_{\parallel h}$ of the hot (“h”) ring current H+ using the pressure parallel to the background magnetic field, $P_{\parallel h}$. Figure 1b shows the anisotropy of the ring current H+, $A_h \equiv P_{\perp h}/P_{\parallel h} - 1$. A rough indicator of the instability of the ring current H+ can be found from $A_h \beta_{\parallel h}^{0.5}$ [Gary and Lee, 1994], but perhaps a better indicator can be

found from the equations of *Blum et al.* [2009], which are based on results by *Gary et al.* [1995]. An instability parameter $\Sigma_h \equiv A_h \beta_{\parallel h}^{\alpha_h}$ is defined. The value of α_h is approximately 0.5, but is more accurately given by the formula of *Blum et al.* [2009] (their equation (3b)). EMIC waves are roughly predicted if Σ_h exceeds the threshold value S_h (defined in *Blum et al.*'s equation (3a)). Note that the threshold S_h is smaller if the cold density is large. Figure 1c shows the cold density from the RAM-SCB simulation, n_c , while Figure 1d shows the ratio of the EMIC instability parameter Σ_h to the threshold value S_h .

Where Σ_h/S_h is large, EMIC waves driven by the ring current H+ population are most likely to be unstable. In Figure 1d, the solid white curve is the threshold value $\Sigma_h/S_h = 1$. In principle, these results indicate that EMIC waves could be driven anywhere outside of this curve, that is, in much of the magnetosphere extending from noon to midnight local time. On the other hand, the theory of *Gary et al.* [1995] was for a plasma consisting only of ring current and cold H+. Here we used $n_c + n_h$ for the value of n_e in their equations (treating all cold particles as cold H+), and neglected the heavy ion ring current particles. It's likely that the heavy ions lead to a reduction in the growth rate of the EMIC waves [see, for instance, *Denton et al.*, 1992], so a larger value than $\Sigma_h/S_h = 1$ may be required for EMIC wave growth. Certainly, however, the regions with very large Σ_h/S_h (orange and red color in Figure 1d) are very likely to be unstable to EMIC waves. Examination of Figure 1 shows that the most unstable regions combine large A_h and to a lesser extent large $\beta_{\parallel h}$ with large n_c . (The dependence on $\beta_{\parallel h}$ is weaker than that on A_h because of the exponent α_h in $\Sigma_h \equiv A_h \beta_{\parallel h}^{\alpha_h}$.)

We will be examining the instability at the MLT = 18 meridian (at dusk local time) which extends upward from the center of the Earth in each of the panels in Figure 1, and

is shown by the vertical solid white line in Figure 1a. Figure 1d shows that, based on local instability, the region predicted to be most unstable to EMIC waves is between just inside $L = 5$ to $L = 6$.

The fractional thermal ion composition greatly affects the propagation characteristics of EMIC waves and is not explicitly simulated in the Rasmussen model. We consider two models for the cold composition. The first of these, which we call the constant cold composition model, has 77% H+, 20% He+, and 3% O+, as was assumed by *Jordanova et al.* [2008] and *Chen et al.* [2014]. In the second model, the He+ concentration is low (about 3% of the light ion density) and the O+ concentration varies strongly from the plasmasphere, in which the O+ concentration is low, to the plasmatrough, in which the O+ concentration is high. Such varying concentration of O+ is suggested by results of *Takahashi et al.* [2006], *Takahashi et al.* [2008], *Denton et al.* [2011], and *Denton et al.* [2014]. We call this second model the variable cold composition model. These populations are assumed to be isotropic with a temperature of 3eV. For the hybrid code simulations to be described in Section 4, we verified that this temperature did not change appreciably during at least the first 18s of the simulation, so the number of particles in the simulation was sufficient to represent the 3eV velocity distribution.

Figure 2 shows quantities from the RAM-SCB simulation at MLT = 18 (vertical solid white line in Figure 1a) using the constant cold composition model. Here, in addition to the ring current parameters for H+ (solid black curves in Figure 2), we also show the ring current parameters for the ring current He+ and O+ (respectively the blue and red solid curves in Figure 2). As was mentioned previously, despite the large β_{\parallel} and A for ring current O+, we do not see waves in the EMIC O+ band. (Anisotropy in an ion component

can only drive waves in the frequency band corresponding to that ion, or lower frequency bands. Ring current H+ can drive waves in all three EMIC wave bands, but ring current O+ can only drive waves in the O+ band.) So in Figure 2d, we show only the instability ratio Σ_h/S_h for ring current H+. Unlike our calculation of Σ_h/S_h plotted in Figure 1d, here we use only the sum of the ring current H+ and cold H+ densities for the value of n_e used in the formulas of *Blum et al.* [2009].

The two vertical gray lines in Figure 2c roughly delineate the plasmopause. We will refer to the region to the left of the leftmost gray line as the plasmasphere, the region in between the two gray lines as the plasmopause, and the region to the right of the rightmost gray line as the plasmatrough. Based on Figure 1c, what we call the plasmasphere might be called a plasmaspheric plume. But there is little difference between the two when we are considering only a meridional cut. And the plasmaspheric plume is just an extension of the plasmasphere (Figure 1c).

Despite the fact that $\beta_{\parallel h}$ and A_h have a peak at the outer edge of the plasmopause, Σ_h/S_h is strongly affected by the cold density so that it peaks at $L = 5.5$ inside the plasmasphere. Thus based on the local instability condition for H+, the outer region of the plasmasphere would be the location most likely to generate EMIC waves [e.g., *Jordanova et al.*, 2001a], though possibly the density gradient in the plasmopause could play some role [e.g., *Chen et al.*, 2009].

Figure 3 is the same as Figure 2, except that in Figure 3c, the dotted curves now show the cold ion composition for the variable cold composition model. Note that the He+ concentration is low, and the O+ concentration becomes large in the plasmatrough region (region to the right of the rightmost vertical line in Figure 3c).

The instability ratio Σ_h/S_h in Figure 3d is slightly smaller than that in Figure 2d owing to the smaller cold H+ density in the variable cold composition model. But the actual reduction in instability is likely to be greater because, as mentioned above, heavy ion populations can reduce the growth rate of EMIC waves. Based on results by *Denton et al.* [2014], the bulk O+ concentration was probably between 0.1 and 0.4 at geosynchronous orbit in the plasmatrough outside of the plasmaspheric plume. This is significantly higher than that in the constant cold composition model, but lower than the concentration in the variable cold composition model at large L (Figure 3c). That is, the real concentration of O+ was likely between the two extremes of these models.

4. Hybrid Code Simulation Results

4.1. Hybrid Code Results for the Constant Cold Composition Model

Figure 4 shows the evolution of the wave power with respect to spatial location for the constant cold composition model. The wave power is shown for rows labeled “A”, “B”, “C”, etc, for the ranges of time listed on the right side of each row versus L shell on the horizontal axis and the parallel coordinate q on the vertical axis. The wave power in the He+ band is shown in the first and third columns (labels “a” and “c”), the wave power in the H+ band is shown in the second and fourth columns (labels “b” and “d”), and the wave power integrated over all frequencies is shown in the rightmost column (“e”). The wave power is normalized to the magnitude of the local magnetic field at each location such that a total wave amplitude equal to the total field would have unity power. Therefore a normalized wave power of 0.01 would correspond to an amplitude of 10% of the background magnetic field. This normalization tends to enhance the apparent wave power at large L and small q where B is smaller relative to other regions. The maximum

normalized wave power in each panel is shown at the upper right under the panel label,
and the wave power is higher than 0.01 at some locations in row “B” only.

The last three columns show the power in grayscale with the constant scale shown at
the right side of each row. The range of color in these panels extends up to 0.003, which
is lower than the maximum power in some panels, so in these cases, the grayscale may
be oversaturated at some locations. This occurs in rows “B”, “C”, and “F”. But, as
indicated, the maximum wave power can be found under the label.

The first two columns “a” and “b” in Figure 4 use a two-dimensional color scale intro-
duced by *Hu and Denton* [2009]. Maximum saturation (intensity or non-whiteness) of the
color corresponds to the maximum wave power in each panel, while the specific hue (or
color) corresponds to ellipticity using the scale at the top left of the figure. The ellipticity
 ϵ is equal to -1 for left hand polarized waves, 0 for linearly polarized waves, and +1 for
right hand polarized waves. Note from the color scale for ϵ that blue color indicates values
of ϵ ranging from -1 to -0.5 and red color indicates values of ϵ ranging from +0.5 to +1.
So blue color does not necessarily represent a purely left hand circularly rotating wave.

While the panels using the 2D color scale can be used to find the region of largest
wave power in the frequency band at a particular time, they do not give a good idea
of whether that wave power is significant. For instance, the maximum wave power in
Figure 4Ab and Ad is only 0.00033, corresponding to a wave amplitude of about 1.8%
of the background magnetic field. But there are regions of strong saturated color in
Figure 4Ab. The predominance of the red color in most of the panel results from whistler
noise, which is right hand polarized. So to judge the wave power, it is easier to use the
right three panels with the same scale or the amplitudes in the top right of each panel.

The roughly vertical curves in each panel show flux surfaces (magnetic field lines) extending from the equatorial L values at the inner and outer edge of the plasmopause as indicated in Figures 2 and 3. If the background magnetic field were exactly dipolar, these curves would be exactly vertical. The approximately horizontal curves show constant values of MLAT at 10° , 20° , 30° , and 40° , with the lowest value of MLAT at small q .

Figure 4 shows that the largest region of wave growth is in the plasmasphere (region to the left of the leftmost nearly vertical curve in each panel), though there are also small regions of quite large wave power elsewhere, such as at the outer edge of the plasmopause in the H+ band in panels Bb and Bd, and in the plasmatrough in the He+ band in panels Fa and Fc.

Figure 5 shows the average wave power in four regions versus the normalized wave frequency ω/Ω_{cp0} , where Ω_{cp0} is the proton gyrofrequency at the magnetic equator found by mapping the magnetic flux calculated using the average magnetic field down to the equator. These are calculated for the time intervals shown at the right side of the figure for the rows labeled “A”, “B”, etc. As was done for Figure 4, the wave power at each point in the simulation has been normalized to the local magnetic field. Then the wave power is averaged in four regions over the simulation grid points. The power is plotted versus unit ω/Ω_{cp0} , such that an integral of the power with respect to ω/Ω_{cp0} would yield the average normalized power in the entire region (including all latitudes).

The average power for the plasmasphere (region to the left of the nearly vertical curves in each panel of Figure 4) is shown in the first column of panels in Figure 5 labeled “a”; the average for the plasmopause (region in between the nearly vertical curves in each panel of Figure 4) is shown in the second column of panels labeled “b”; the average

for the plasmatrough (region to the right of the nearly vertical curves in each panel of Figure 4) is shown in the third column of panels labeled “c”; finally the average over the entire simulation domain is shown in the last column of panels labeled “d”. The blue curves show the left hand polarized wave power, while the red curves show the right hand polarized wave power. The value of ϵ at any point is $(A_+ - A_-)/(A_+ + A_-)$, where $A_{\pm} \equiv \sqrt{P_{\pm}}$, and A_{\pm} and P_{\pm} are the amplitude and wave power, respectively, with $+$ for the right hand polarized wave power, and $-$ for left hand polarized wave power. Thus if the blue curve is higher than the red curve, $P_- > P_+$, $\epsilon < 0$, and the waves are left hand polarized.

The two vertical gray lines are at the O+ gyrofrequency, $\omega/\Omega_{cp0} = 1/16$, and the He+ gyrofrequency, $\omega/\Omega_{cp0} = 1/4$. The low amplitude wave power under 10^{-4} that is fairly constant with respect to frequency is thermal noise. The EMIC waves show up as peaks rising from this background. Early in the growth cycle of the waves, such as at the first time interval, $t = 10$ to 35 s in the first row labeled “A”, the wave power is left hand polarized (blue curves higher than red curves). There are peaks with respect to frequency in the He+ band (region in between the two gray lines) and in the H+ band (region to the right of the rightmost gray line) in all spatial regions, but the He+ wave power is strongest in the plasmasphere while the H+ wave power is strongest in the plasmopause and plasmatrough.

By examining Figure 5 column d with wave power averaged over all spatial regions, we see that the largest wave power is generally in the He+ band, as was roughly evident comparing columns c and d of Figure 4. As time progresses, the He+ waves grow to a

maximum (Figure 5Bd), then decrease in power and become more linearly polarized as indicated by the red curve coming closer to the blue curve in Figure 5Gd.

In the plasmasphere (column a of Figure 5), there is some small wave growth in the H+ band at $\omega/\Omega_{cp0} \sim 0.47$; this is most evident in the 35s to 60s interval (Figure 5Ba). But the largest wave power in the plasmasphere is always in the He+ band, and in this frequency band, the wave power in the plasmasphere is always the dominant component of the total wave power (comparing columns a and d of Figure 5).

The frequency dependent evolution of wave power in the plasmatrrough (Figure 5 column c) is different. At the earliest time interval 10s to 35s (row A), EMIC waves start to grow in the H+ band at $\omega/\Omega_{cp0} = 0.5$ (Figure 5Ac). In the next time interval 35s to 60s (Figure 5Bc), the strongest wave power has shifted to lower frequency, but still within the H+ band at $\omega/\Omega_{cp0} \sim 0.33$. Later during the time interval 110s to 160s (Figure 5Ec and Fc), the most intense wave power is in the He+ band. At these times, the strongest wave power is centered at about $\omega/\Omega_{cp0} = 0.2$, which is a higher normalized frequency than the He+ band waves in the plasmasphere that are centered at a frequency of about 0.17 (Figure 5 column a).

The frequency dependent evolution of wave power in the plasmopause (Figure 5 column b) is intermediate between that in the plasmasphere and plasmatrrough (columns a and c, respectively). Wave power grows in the He+ band from the earliest time centered at a frequency intermediate between that in the plasmasphere and in the plasmatrrough. Wave power grows in the H+ band at early times (Figure 5Ab and Bb) similar to that in the plasmatrrough (Figure 5Ac and Bc). The reason that the wave power in the plasmopause is similar to that in the plasmasphere and plasmatrrough can be easily seen from Figure 4.

The He+ wave power in the plasmopause is the outermost extension of the He+ wave power in the plasmasphere (Figure 4Bc and Cc), and the strongest H+ band wave power is at the boundary between the plasmopause and plasmatrough (Figure 4Bd). These simulation results suggest that the wave growth in the plasmopause is not predominantly due to the density gradient, which would be largest at the center of the plasmopause (Figure 2c), but rather due to the favorable properties (discussed later) of the adjacent spatial regions.

4.2. Hybrid Code Results for the Variable Cold Composition Model

Now we show hybrid code simulation results for the variable cold composition model. Recall that there are two main differences between the two models, as illustrated in Figure 2c and Figure 3c. In the variable cold composition model, the He+ composition is much lower, about 3% of the cold light ions versus 20% of all the cold particles, and the O+ composition is much higher, becoming dominant at the largest L shells.

Figure 6 shows the evolution of the wave power with respect to spatial location using the same format as Figure 4. One difference is that the time intervals in Figure 6 are 20s rather than the 25s intervals used in Figure 4. (This choice was made because the significant wave evolution occurred during a shorter total amount of time for the variable cold density composition model.) The wave evolution in this case is simpler. The He+ band waves are confined to the plasmasphere, and the H+ waves are strongest near the inner edge of the plasmopause, extending from the outer third of the plasmasphere (Figure 6 column d, especially panel Bd) to the inner third of the plasmopause (especially panels Bd and Cd). There is no significant wave growth in the plasmatrough. The maximum normalized

457 wave power is lower, reaching a maximum value of 0.0036 in Figure 6Be versus 0.013 in
 458 Figure 4Be. Furthermore the apparent wave power decays more quickly.

459 This apparent decay in wave power is somewhat misleading. As the waves propagate
 460 along the magnetic field toward the ionospheric boundary, the normalized wave power
 461 decreases due to the increase in the background magnetic field. There is some energy
 462 loss near the ionospheric boundary due to the resistive layer that is there, but results
 463 by *Hu et al.* [2010] suggest that there is also significant reflection of wave power. There
 464 is a pileup of energy near the grid scale in the radial direction at later times. Electron
 465 Landau damping, not included in our simulation, would probably reduce the power of
 466 these significantly oblique waves [*Thorne and Horne, 1992*].

467 Another difference between Figure 4 and Figure 6 is that the waves in Figure 6 appear
 468 to be more linearly polarized. The left hand polarized waves tend to be more cyan colored
 469 than blue and the right hand polarized waves tend to be more yellow colored than red.
 470 We do not have an explanation for this other than to note that it is consistent with linear
 471 theory. Calculating the wave properties at $L = 5.5$ (within the plasmasphere) at the k_{\parallel}
 472 value of maximum growth rate but for $\theta_{kB} = 30^\circ$, we find that the ellipticity is -0.72 for
 473 the constant cold composition model and -0.55 for the variable cold composition model.
 474 The fact that the waves are more linearly polarized for larger O+ concentration was also
 475 noted by *Hu et al.* [2010].

476 Figure 7 shows results from the same simulation with respect to frequency, with the
 477 same format as Figure 5. As we saw from Figure 6, most of the He+ wave growth was
 478 in the plasmasphere (see Figure 7 column a). (There is a very small peak in power in
 479 the He+ band in the plasmopause which can be seen in Figure 7Db as the small peak

just to the left of the rightmost vertical gray line.) Waves in the H+ band grow in the
 plasmasphere and plasmopause regions. There is a slight shift to lower frequency at later
 time, as can be seen by comparing Figure 7Bb to Figure 7Cb.

5. Discussion and Summary

5.1. Effect of the Plasmopause

While there may be significant wave growth within the plasmopause, that growth does
 not seem to result from the density gradient. The growth in the plasmopause occurs
 in a region that either extends across the plasmopause boundary into the plasmasphere
 (Figure 4Bc and Figure 4Cc) or into the plasmatrough (Figure 4Bd). The region of
 steepest gradient (middle of the plasmopause region) seems to be dispreferred for wave
 growth.

The idea that a density gradient guides the wave so that the wave vector remains
 approximately aligned with the magnetic field leading to larger wave growth has been
 supported by *Thorne and Horne* [1997], *Chen et al.* [2009], and *de Soria-Santacruz et al.*
 [2013] using the ray tracing technique. *Thorne and Horne* [1997] show guiding near the
 inner edge of the plasmopause. The mechanism seems to be that the waves are refracted
 inward while in the plasmopause. But after the waves propagate into the plasmasphere,
 they refract outward. Bounces in position and wave angle can occur (see Thorne and
 Horne's Figure 3). *Chen et al.* [2009] and *de Soria-Santacruz et al.* [2013], on the other
 hand, describe guiding within a gradient on a localized density perturbation. Figure 2 of
Chen et al. [2009] shows that the wave growth is strongest at the outer (high beta) edge
 of the peaks in electron density n_e . This might cause one to wonder if the larger growth
 in their simulation can be explained entirely by local conditions. However, experiments

501 varying the density profile show that if the density profile is varied so that the local density
 502 is everywhere smaller but the density gradient is larger, the wave growth increases (Lunjin
 503 Chen, private communication, 2014). Therefore the density gradient is playing a role in
 504 the wave growth in Chen et al.’s simulations.

505 Figure 1c of *de Soria-Santacruz et al.* [2013] more clearly shows maximum wave growth
 506 near the peak in the density gradient. *de Soria-Santacruz et al.* [2013] state that “guiding
 507 is possible for irregularity sizes on the order of the EMIC wave length.” In their model,
 508 the drop in density is a factor of about 2.5 within a width of somewhat less than about
 509 two parallel wavelengths. In our simulation, the drop in density is a factor of about 4.5
 510 within a plasmopause width of slightly less than four parallel wavelengths. Therefore the
 511 parameters are fairly similar.

512 One factor that is not included in the ray tracing simulations is the radial structure of
 513 the waves. *Hu and Denton* [2009] found that there was a radial coherence length over
 514 which the EMIC waves would maintain a coherent structure. Within the plasmopause, the
 515 parallel wavelength and frequency of the waves vary (as described below in Subsection 5.3),
 516 and it may be that coherent growth of EMIC waves is difficult within a steep gradient.

517 Despite the fact that the major wave growth is not within the plasmopause, the plasma-
 518 pause does appear to play a significant role in the evolution of the direction of the local
 519 wave vector. Figure 8 shows for the constant cold composition model the s component of
 520 the wave magnetic field, B_s , normalized to the equatorial magnetic field at the central L
 521 shell, B_0 , in the meridional plane of the simulation plotted using Cartesian coordinates
 522 so that the angle between the wave vector (normal to the wave fronts) and magnetic field
 523 can be roughly estimated. Each panel shows B_s/B_0 at the central time of one of the first

five time intervals plotted in Figure 4. The green curves that intersect $Z = 0$ are magnetic flux surfaces at the plasmapause boundaries shown in Figure 2. Note carefully that the curves of constant MLAT (curves roughly normal to the flux surfaces) are not normal to the flux surfaces and cannot be used to judge the wave power angle. The equilibrium magnetic field roughly follows the shape of the flux curves and the shape of the outer boundaries L boundaries which are also flux surfaces.

Note from Figure 8A, corresponding to $t = 22.5$ s, that the largest early wave growth is in the plasmasphere (region to the left of the leftmost green curve intersecting $Z = 0$), marked by point “P”. In Figure 8A, the dominant wave power is at MLAT less than 10° and the wave fronts are roughly normal to the magnetic flux surfaces indicating that the wave vector is roughly parallel to those surfaces. At $t = 47.5$ s (Figure 8B), the dominant wave power is still within the plasmasphere, and for small MLAT, the wave vector is still roughly along the equilibrium magnetic field. But at larger MLAT, especially for MLAT $> 10^\circ$, the wave vector is tilted relative to the equilibrium magnetic field. Well within the plasmasphere, at point “Q” in Figure 8B, the wave vector has refracted outward. This is even clearer at point “R” in Figure 8C and point “S” in in Figure 8D. Later waves in the plasmatrough, marked by point “T” in in Figure 8E also appear to be refracting outward.

But even though the dominant wave power is within the plasmasphere at $t = 47.5$ s (Figure 8B), the wave fronts close to the inner plasmapause boundary are tilted inward; see point “U” in Figure 8B. Inward refraction within the plasmapause is evident just outside the inner plasmapause boundary near point “U” and is also evident that points “V” and “W” in Figure 8C and D, respectively. The fact that the wave front within the plasmasphere is also refracted inward (point “U”) suggests that the wave fronts are affected

globally by the surrounding region. The weaker but faster propagating waves outside the inner boundary of the plasmapause in Figure 8B appear to be dragging forward the wave fronts within the plasmasphere. The result may be similar to that of the radially bouncing wave packets of *Thorne and Horne* [1997].

5.2. Wave Normal Angles

As we indicated earlier, the wave normal angle θ_{kB} can be roughly estimated from Figure 8 as the angle between the normal to the wave fronts and the magnetic flux surfaces. For waves within the plasmasphere and plasmatrrough, θ_{kB} appears to be usually within 25° of zero for $\text{MLAT} \leq 10^\circ$. At larger values of MLAT, this angle increases. For instance, at point “R” in Figure 8C (at about 14°), the angle is about 40° . The largest values of θ_{kB} occur in the plasmapause where there is a steep gradient in the frequency of the waves (as described in Section 5.3 below). At point “W” in Figure 8D, θ_{kB} is about 60° and farther along on the same flux surface at $\text{MLAT} > 20^\circ$ θ_{kB} is about 85° .

For the constant cold composition model at $L = 5.75$ (middle of plasmapause) at the magnetic equator, the local linear growth rate of EMIC waves is maximum for $\theta_{kB} = 0^\circ$ (parallel propagation). The growth rate decreases to one half of its maximum value at about $\theta_{kB} = 27^\circ$, to 1/10 of its maximum value at $\theta_{kB} = 44^\circ$, and to zero value (marginal stability) at $\theta_{kB} = 76^\circ$. At $\theta_{kB} = 85^\circ$, the damping rate is about $-0.0015 \Omega_{cp}$. The damping rate is likely to be larger at high MLAT where the plasma is less unstable.

5.3. Frequency of the Waves

Generally, we find that the He+ band waves with lowest frequency are most unstable in the plasmasphere (Figure 5), whereas the H+ band waves with higher frequency are

most unstable farther out. In Figure 4, the H+ band waves are most unstable in the
 plasmopause and plasmatrough, and particularly near the outer edge of the plasmopause
 (Figure 4Bd). In Figure 6, we find that the H+ band waves occur at the outer edge of
 the plasmasphere and inner portion of the plasmopause (Figure 6Bd). As we will discuss
 below, this difference is due to the vastly different cold ion composition. But we see
 in both cases a preference for H+ waves relative to He+ waves at larger L . Note that
Anderson et al. [1992b] found that ω/Ω_{cp} (their “X”) increased with respect to L (their
 Figure 5, top panel).

In addition, there is a tendency for the wave frequency of the waves that are driven
 to gradually decrease with respect to time. For instance, we see in column c of Figure 5
 (plasmatrough) that at first the most unstable waves are at $\omega/\Omega_{cp} = 0.5$, then later at
 about 0.33, and even later at about 0.2.

Both of these dependencies can be easily understood. Assume that the waves are driven
 by a bi-Maxwellian distribution of hot protons such that the wave is in Doppler resonance
 with Ω_{cp} for the hot protons with a parallel velocity equal to the parallel thermal speed
 of the hot protons, $v_{th||h} \equiv \sqrt{2k_B T_{||h}/m_p}$, so that

$$\Omega_{cp} = \omega + k_{||} v_{th||h}. \quad (1)$$

Here k_B is the Boltzmann constant, and $T_{||h}$ is the hot proton temperature associated
 with motion along the magnetic field. From (1), we find

$$\left(\frac{1 - \bar{\omega}}{\bar{k}_{||}} \right)^2 = \bar{v}_{th||h}^2 \quad (2)$$

$$= \frac{n_e}{n_h} \beta_{||h} \quad (3)$$

$$\equiv \beta_{||h,e}. \quad (4)$$

Here the overbars indicate normalized quantities, where we have normalized distances to c/ω_{pp} and inverse time to Ω_{cp} , and where the proton plasma frequency is $\omega_{\text{pp}} \equiv \sqrt{n_e e^2 / m_p \epsilon_0}$, the proton cyclotron frequency is $\Omega_{\text{cp}} \equiv eB/m_p$, e is the proton charge, m_p is the proton mass, and ϵ_0 is the vacuum permittivity. The quantity $\beta_{\parallel \text{h,e}}$ is the plasma beta calculated using the parallel temperature of the hot protons and the total electron density. (This quantity was used by *Gary et al.* [1994b].)

For a multi-species plasma with singly charged ions of species s , the dispersion relation for electromagnetic ion cyclotron waves is [Swanson, 2003, p. 28]

$$\bar{k}_{\parallel}^2 = \bar{\omega} \left(\sum_s \frac{\eta_s}{1 - \bar{m}_s \bar{\omega}} - 1 \right). \quad (5)$$

Here the species concentration $\eta_s \equiv n_s/n_e$, and the normalized ion mass $\bar{m}_s \equiv m_s/m_p$. If we substitute this into (4), we find

$$\frac{\bar{\omega}}{(1 - \bar{\omega})^2} \left(\sum_s \frac{\eta_s}{1 - \bar{m}_s \bar{\omega}} - 1 \right) = \frac{1}{\beta_{\parallel \text{h,e}}}. \quad (6)$$

We will show that this equation predicts the most unstable frequencies of EMIC waves remarkably well. Note that in terms of normalized parameters, it is not the absolute total density that determines $\beta_{\parallel \text{h,e}}$, but the ratio n_e/n_h , since $\beta_{\parallel \text{h,e}} \equiv (n_e/n_h)\beta_{\parallel \text{h}}$.

Within each EMIC wave band, the left hand side of (6) increases with respect to $\bar{\omega}$, and aside from frequencies close to the resonant frequencies, $\bar{m}_s \bar{\omega} = \omega/\Omega_{\text{cs}} = 1$, and the cutoff frequencies where $k_{\parallel} = 0$, the left-hand side of (6) increases with respect to $\bar{\omega}$ across wave bands. This is demonstrated in Figure 9 for the case of the concentrations in our constant cold composition model, $\eta_{\text{H}} = 0.77$, $\eta_{\text{He}} = 0.20$, and $\eta_{\text{O}} = 0.03$. (The left-hand side of (6) goes to infinity where $\omega/\Omega_{\text{cs}} = 1$ and to zero where $k_{\parallel} = 0$.)

An increase in n_e results in a larger value of $\beta_{\parallel h,e}$, and hence a lower value for the right-hand side of (6), which means that (6) will be satisfied for lower values of $\bar{\omega}$. This explains why the He+ band in our simulations is preferably driven in the plasmasphere, while the H+ band is preferably driven in the plasmatrough (Figure 4, row B).

While (6) shows that the frequency of the unstable waves is dependent on $\beta_{\parallel h}$, but not on the anisotropy of the hot population $A_h \equiv T_{\perp h}/T_{\parallel h} - 1$, these quantities are not usually independent. A plasma with large $\beta_{\parallel h}$ and large A_h would be extremely unstable. Usually the hot population stays close to a threshold similar to $\Sigma_h = S_h$ mentioned in Section 3 [Blum *et al.*, 2009]. Thus considering the definition of $\Sigma_h \equiv A_h \beta_{\parallel h}^{\alpha_h}$, the right side of (6) would be expected to be proportional to A_h^{1/α_h} , where α_h is usually between 0.4 and 0.5, showing that normally we expect higher anisotropy to drive higher frequency waves. This expectation is consistent with the upper limit on $\bar{\omega}$ that immediately follows from Equation 2.23 of Kennel and Petschek [1966],

$$\bar{\omega} \leq \frac{A_h}{1 + A_h}. \quad (7)$$

Figure 10 shows the normalized frequency $\bar{\omega} \equiv \omega/\Omega_{cp}$ versus L shell for the constant cold composition model in Figure 10a and the variable cold composition model in Figure 10b. The upper and lower blue curves in Figure 10a or Figure 10b are the predicted most unstable wave frequency based on (6) for the H+ band waves and He+ band waves, respectively. In the cold plasma limit at finite θ_{kB} , the waves in each band below the crossover frequency would connect topologically to the higher frequency mode, with the H+ band waves connecting to the whistler band [Andre, 1985; Hu *et al.*, 2010]. From this perspective, we might need to know whether the wave is above or below the crossover frequency to label the mode. But here we call all waves between the mode gyrofrequency

and the next lower gyrofrequency the name of the higher gyrofrequency. In other words, all waves between the He+ and H+ gyrofrequency are called H+ band waves. Note also that results that we present below suggest that the cold plasma topology is not always relevant.

The blue asterisks in Figure 10 show the frequency of maximum growth rate predicted by the electromagnetic plasma dispersion code Waves in Homogeneous Anisotropic Multicomponent Plasmas (WHAMP) [Ronnmark, 1982], while the blue circles show the frequency of waves actually observed in our simulations at the earliest time and at positions and frequency consistent with Figures 4, 5, 6, and 7. The observed waves in our simulation (circles) are at frequencies very close to the most unstable frequencies predicted by WHAMP (blue asterisks), and both of these are close to those based on the simple model (blue solid curves). From Figure 10, we also see that (6) explains the shift in frequency within each wave band from low values for high n_e at low L to higher values for low n_e at high L .

The shift with respect to time of wave frequency from higher frequency to lower frequency can be explained by the evolution of the hot proton population. The tendency of the waves is to drive the plasma toward isotropy ($T_{\parallel h} = T_{\perp h}$) by transferring thermal energy from the perpendicular to parallel direction [Denton *et al.*, 1993]. But the waves do not drive the plasma toward complete isotropy. Rather they reduce the anisotropy so that the plasma becomes approximately marginally stable to the particular waves that is affecting the plasma [Gary *et al.*, 1994c; Denton *et al.*, 1994]. The high frequency waves transfer energy to the parallel direction, increasing $\beta_{\parallel h}$, and thus leading to conditions that favor lower frequency waves.

5.4. Effect of Varying O+ Composition

Omidi et al. [2013] showed that a high concentration of O+ in an H+/O+ plasma yielded EMIC waves that were heavily damped. They interpreted these results as due to higher harmonic resonance with the O+ ions.

We mentioned in an AGU presentation that high concentration of O+ can eliminate He+ band and H+ band waves [*Denton and Hu*, 2010], and we observed that same result here for the variable cold composition model in the plasmatrough (Figure 7 column c). Left hand polarized waves can only grow above the cutoff frequency. For a cold plasma, this frequency can be found from (5) by setting $\bar{k}_{\parallel} = 0$. In Figure 10a and Figure 10b, the cold plasma cutoff frequency for H+ and He+ bands is the dashed red curve, while the upward pointing red triangles are the left hand polarized mode cutoff frequency determined from WHAMP. Clearly, the cold plasma formula well predicts the kinetic cutoff frequency. The red solid curve Figure 10a and Figure 10b shows the maximum possible frequency based on (7), while the dotted horizontal gray line corresponds to $\omega = \Omega_{\text{cHe}}$. Note that the dashed red curve for each wave band represents the lowest possible frequency for that wave mode, while the highest possible frequency is the solid red curve for the H+ band or the dotted horizontal gray line for the He+ band. The blue curves and blue data points always occur within these limits. While we haven't studied this aspect in detail, it also appears that the waves only grow where the blue curve is significantly above the dashed red curve, that is, where the most unstable frequency is significantly above the cutoff frequency.

For the variable cold composition model, Figure 10b shows that the wave frequency for both H+ band and He+ waves based on the simple model (blue curve) and the cutoff

frequency (dashed red curve) get very large in the plasmatrough. At the outer edge of the plasmopause (rightmost gray line in Figure 3c), $\eta_{\text{He}} = 0.032$ and $\eta_{\text{O}} = 0.35$. With those concentrations, the cold plasma He+ cutoff frequency is at $0.23 \Omega_{\text{cp}}$, and the H+ cutoff frequency is at $0.44 \Omega_{\text{cp}}$. The large cutoff frequency means that the range of possible unstable frequencies is small. The predicted most unstable frequencies for these modes (solid blue curves) are even higher. For the He+ band, the predicted most unstable frequency is $0.244 \Omega_{\text{cp}}$, very close to the He+ gyrofrequency at $0.25 \Omega_{\text{cp}}$. The predicted most unstable frequency for H+ is $0.52 \Omega_{\text{cp}}$, close to the upper limit of unstable frequencies given by (7), $0.57 \Omega_{\text{cp}}$. Neither H+ band nor He+ band waves were observed in the plasmatrough.

Note that the cutoff frequency in the H+ band above the He+ gyrofrequency is not necessarily determined by the He+ concentration. This is true also for the most unstable frequency. As mentioned above, with $\eta_{\text{He}} = 0.032$ and $\eta_{\text{O}} = 0.35$, the cold plasma cutoff frequency in the H+ band is at $0.44 \Omega_{\text{cp}}$. If we drop η_{He} to zero (by increasing η_{H}), we get $0.35 \Omega_{\text{cp}}$, but if we drop η_{O} to zero, we get $0.27 \Omega_{\text{cp}}$. Thus in this case O+ is playing the dominant role in determining the H+ cutoff frequency, and hence the width in frequency of the stop band (region with no possibility of waves) above Ω_{cHe} . Consequently we advise that researchers use caution about using the stop band at $\omega > \Omega_{\text{cHe}}$ alone to estimate the He concentration, especially at solar maximum (see discussion below).

The effect of heavy ions on the EMIC wave frequency can be easily understood based on (6) and (5). Assume that we vary the composition but hold the total density constant so that the right hand side of (6), equal to $1/\beta_{\parallel \text{h,e}}$, is constant. The left hand side of (6) has a product of two terms. The first of these, $\bar{\omega}/(1 - \bar{\omega})^2$, increases with respect to $\bar{\omega}$.

The second of these is $\sum_s \eta_s / (1 - \bar{m}_s \bar{\omega}) - 1$, which can be expressed as

$$\sum_s \frac{\eta_s}{1 - \bar{\omega}^s} - 1, \quad (8)$$

where $\bar{\omega}^s \equiv \bar{m}_s \bar{\omega} = \omega / \Omega_{cs}$ is the angular frequency normalized to the species gyrofrequency. The second term has quantities $\eta_s / (1 - \bar{\omega}^s)$. These terms are positive if $\bar{\omega}^s$ is less than unity, and negative if $\bar{\omega}^s$ is greater than unity. So these quantities are negative for a heavy ion species with gyrofrequency below the wave band. That is, He+ and O+ have gyrofrequencies below the H+ band for which the wave frequency is greater than Ω_{cHe} , and O+ has a gyrofrequency below the He+ band for which the wave frequency is greater than Ω_{cO} . Thus increasing the concentration of the heavy ions with gyrofrequency below the waveband will decrease the second term, and then the wave frequency will have to increase in order that (6) continue to be satisfied. So when we increase η_{O} , the most unstable frequency for EMIC waves will increase for both He+ and H+ bands.

Similarly, the cutoff frequency can be found by setting the right-hand side of (5) equal to zero (so that $\bar{k}_{\parallel} = 0$). Comparing (5) and (8), we see that the cutoff frequency is found from solutions of (8) equal to zero (except for the O+ band with cutoff at $\omega = 0$). In order for there to be a valid solution, the sum of positive terms $\eta_s / (1 - \bar{\omega}^s)$ for species with gyrofrequency above the waveband must be at least a value unity greater than the negative terms for species with gyrofrequency below the waveband. If the concentration is increased for a heavy ion with gyrofrequency below the waveband, increasing the magnitude of the negative terms, the frequency must adjust to increase the magnitude of the positive terms. Those will become greater if $\bar{\omega}$ increases. For instance, the H+ term is $\eta_{\text{H}} / (1 - \bar{\omega})$, and this increases as $\bar{\omega}$ increases. Similarly the magnitude of the negative terms will decrease

as $\bar{\omega}$ is increased. So when we increase η_{O} , the cutoff frequencies for both He+ and H+ EMIC wave bands will also increase.

In the variable cold composition case, there is some small wave growth at the inner edge of the plasmopause. This appears to be largest in the H+ band (Figure 6Bd and Cd), but does occur to a smaller degree in the He+ band (Figure 6Da and Ea). At the inner edge of the plasmopause, $\eta_{\text{He}} = 0.038$ and $\eta_{\text{O}} = 0.091$ (at leftmost gray line in Figure 3c). For these concentrations, the He+ cutoff frequency is at $0.13 \Omega_{\text{cp}}$, and the H+ cutoff frequency is at $0.30 \Omega_{\text{cp}}$. The predicted most unstable frequency for each mode is significantly higher than the cutoff frequency, and well under the upper frequency limit for each mode. Thus the limits are not so extreme, and Figure 7 column b shows small wave growth in both bands within the plasmopause.

In conclusion, it appears that a large concentration of O+ can severely limit EMIC waves. Based on results summarized by *Denton et al.* [2011], there is usually a small concentration of O+ in the plasmasphere during all phases of the solar cycle, but the concentration of O+ in the plasmatrough varies greatly. During solar maximum, η_{O} may be around 0.35 on average in the plasmatrough, but at solar minimum there is very little O+ in the plasmatrough. These results suggest that there is usually very little O+ at geostationary orbit during solar minimum. Our preliminary results studying the more detailed dependence of η_{O} [*Denton et al.*, 2012] suggests that the O+ concentration is greatest at dawn local time (where the plasma is more “plasma cloak-like” [*Chappell et al.*, 2008; *Lee and Angelopoulos*, 2014]) and where it is less “plasmasphere-like” (high density) and where EMIC waves are less likely to occur [*Anderson et al.*, 1992a; *Halford*

et al., 2010]). These results also suggest that the O+ concentration is higher at times of large negative Dst.

At any rate, these results suggest that, all other things being equal, EMIC waves would be more likely in the plasmatrough at solar minimum. Of course, “all other things” are not always equal. But under conditions conducive to EMIC waves, especially large A_h and $\beta_{||h}$, possibly enhanced by large n_e , EMIC waves should be more likely in the plasmatrough during solar minimum than at solar maximum.

Recent results by *Lee and Angelopoulos* [2014] suggest that under some circumstances, the He+ concentration can be much higher than that assumed in either of our models. (See their Figure 7.) For the case described in this paper, at geostationary orbit at MLT = 18, they find on average a low concentration of He+. But at large distances on the nightside, and to a lesser extent in the morning local time sector, they find that the He+ concentration can be quite large, and that would also potentially have dramatic effects on the EMIC wave properties.

5.5. Kinetic Effects on the Dispersion Relation

EMIC waves are thought to occur most often in the left hand polarized wave surface above the crossover frequency. In Figure 10, the crossover frequency based on a cold plasma is indicated by the dotted green curves using the formula of *Ubersoi* [1973]. The green squares indicate the kinetic crossover frequency found using WHAMP. There are only two of these points shown. In other cases, we were not able to solve for the right hand polarized waves using WHAMP. We find that sometimes the waves are driven below the crossover frequency, for instance for the H+ band waves at the outer edge of the plasmopause in the constant cold composition model. From Figure 10a, we see that the

green square at $\bar{\omega} = 0.53$ is definitely above the blue circles (denoting the observed waves in the simulation at the earliest time).

Figure 11 shows the real frequency $\omega/\Omega_{\text{cp}}$ and normalized growth rate $\gamma/\Omega_{\text{cp}}$ on the left hand polarized wave surface. Noting the range of red color, indicating positive growth rate, it is clear that the waves are growing at frequencies below the kinetic crossover frequency at $\bar{\omega} = 0.53$. In this case, the crossover frequency is near the upper edge (near the high values of k_{\parallel}) of the region in \mathbf{k} space that is unstable. An interesting feature of this wave surface is that it maintains its topological integrity at large values of θ_{kB} . Based on cold plasma theory, we would expect the part of this surface above the crossover frequency value to connect topologically to the right hand polarized surface at smaller k_{\parallel} [Andre, 1985; Hu et al., 2010]. But this surface is entirely left hand polarized. Running WHAMP with $\log_{10}(k_{\perp}\rho_{\perp}) = -1$, and stepping $\log_{10}(k_{\perp}\rho_{\parallel})$ with the last solution as an input to the next, we are not able to get the solution to jump from the left hand polarized surface to the right hand polarized surface, even with logarithmic steps in $\log_{10}(k_{\perp}\rho_{\parallel})$ as small as 10^{-5} . Examination of the right hand polarized surface in this frequency range (not shown) indicates that it exists as a significantly damped mode at small values of k_{\perp} , and at larger values of k_{\perp} it is heavily damped as it approaches the crossover frequency so that WHAMP is not able to converge on a solution. Note that WHAMP converges on the nearest complex frequency to the input frequency, so the imaginary part of the frequency does influence the solutions that it finds. Evidence that the left and right hand polarized surfaces are changing from the cold plasma situation may be that the green squares in Figure 10 are significantly off from the dotted green curves.

We varied the temperature of the various species to find out what is causing the anomalous dispersion surfaces. If we set the temperature of all the species except ring current H+ equal to 0.1 eV, the dispersion surfaces are like we have described above, including that plotted in Figure 11. If we then lower the ring current H+ temperature to 0.1 eV, we get the cold plasma dispersion surfaces including the transition at the crossover frequency from left-hand to right hand polarized waves. This shows that in our case it is the finite temperature of the ring current H+ that is causing the anomalous behavior.

This shows that cold plasma theory does not always accurately describe the topology of the wave surfaces, as in this case, it clearly didn't. Such a result may have severe implications for ray tracing calculations. *Chen et al.* [2011] studied a H+/He+ plasma and came to a similar conclusion. Their Figure 1e appears to show a change in connection of surfaces as θ_{kB} is varied, which we do not observe, but our surface with $\omega > \Omega_{cHe}$ is similar to their upper dashed red curve for $\theta_{kB} = 15^\circ$. *Chen et al.* [2011], however, reported that their results depended on "warm" temperature for the He+, whereas we are finding differences from cold plasma theory with hot ring current H+ but very cold He+.

5.6. Cycle of Wave Growth

In 2007, there was a debate about the evolution of EMIC waves. *Thorne and Horne* [2007] argued that EMIC waves complete their full wave growth in one transit toward the ionosphere and then, as they become oblique, are heavily damped by electron Landau damping so that no significant wave power is reflected. *Khazanov et al.* [2007] argued that the waves do not complete their growth in a single transit and that there is some reflection of wave power.

In our case, the waves do complete their growth in one transit toward the ionosphere, apparently favoring the position of Thorne and Horne, even without Landau damping being included in the model. On the other hand, the plasma instability will not always be as strong as it is in the case that we are simulating, and the noise level in our simulation is larger than that in the real magnetosphere. So under more realistic conditions, the waves will need more time to grow to large amplitude.

Secondly, we do see reflected wave power, albeit at an amplitude decreasing with respect to time. This can be seen in Figure 6, columns a and b, but can be seen better in the results presented by *Hu et al.* [2010]. This result would seem to favor the position of Khazanov et al. But we do not have electron Landau damping in our simulation. This would damp the waves at later times, especially considering that the scale lengths in radial structure of our late time waves are moving toward grid scale corresponding to highly oblique waves. Therefore our results, while relevant to this debate, are inconclusive, and more work will need to be done in order to understand the realistic temporal evolution of the waves.

5.7. Comparison of Observed and Simulation Wave Spectra

Examination of Figures 4 and 6 shows the EMIC wave power and relative contribution from the He+ and H+ bands will vary greatly depending on the spatial location, and Figure 5 shows that the frequency spectrum can change with respect to time during an EMIC event. Comparison of the results in our two runs shows that the wave power and frequency spectrum depends strongly on the ion composition, and (6) shows that the wave frequencies that are likely to be driven are dependent on the hot proton temperature and the cold proton density. Thus it will be difficult to do an exact comparison between observations and model results unless a complete set of observations is available including

composition of hot and cold ions. In addition, no spacecraft was at the exact local time of our simulation ($\text{MLT} = 18$) at the exact time of the simulation (June 9, 2001, 1900 UT).

For our purposes here, we simply show that at one location in the region of largest wave growth the kind of wave spectra that results from our simulation is similar to spectra that are observed. *Fraser et al.* [2005] showed EMIC wave spectra at several times during June 9, 2001 (their Plate 2 and Figure 5). Here we plot in Figure 12a the waves observed by the GOES 10 spacecraft at June 9, 2001, 2140–2150 UT when the spacecraft was at $\text{MLT} = 13$, which Fraser et al. plotted in their Figure 5 (top right panel). Based on their Figure 6, GOES 10 may have been in a high density region at that time (see the 01A and 080 tracks on their figure). The data was windowed, and three point frequency averaging was applied.

In Figure 12b, we show a wave spectrum from the variable composition simulation at $t = 20\text{s}$ to 55s (a smaller interval than was used for Figure 12a) at $L = 5.3$ and $\text{MLAT} \sim 8^\circ$. This location is in the plasmasphere where both He^+ mode and H^+ mode waves are observed and the polarization is mostly left-handed (Figure 6, row B). This is also the time of maximum wave power (Figure 6 and Figure 7). There are strong similarities between the observed and simulated frequency spectra. Both spectra show peaks in He^+ band and H^+ band wave power. The waves are dominantly left hand polarized in both cases, though linearly polarized at the low frequency end of the H^+ band waves. Observed GOES spectra calculated during smaller amounts of time (not shown) generally have sharper frequency peaks with larger wave power and may have different polarization properties. For instance, during some smaller time intervals, the entire H^+ peak had left-hand or linear polarization.

There are some significant differences between the observed and simulated frequency spectra. The wave power for the simulated spectrum is larger. The wave amplitude in the simulation is about 10% of the background magnetic field, which is large, but not unrealistically so. In the simulation, the wave power in the H+ band is much larger compared to that in the He+ band than for the observed waves. Based on Figure 6, row B, the ratio of wave power in the He+ and H+ bands would vary greatly depending on the exact spatial location. There is significant wave power observed by GOES 10 in the O+ band (to the left of the leftmost vertical gray line in Figure 12a), apparently linearly polarized, whereas we do not observe that in the simulation (Figure 12b). Perhaps the most significant difference in the two spectra is the noise level. Our numerical noise level, normalized wave power $\sim 10^{-4}$ is much larger than the observed noise level $\sim 10^{-7}$. Both the He+ band and H+ band wave spectra are well above the numerical noise, indicating that they are well represented, but the wave power at higher frequencies is too large.

5.8. Summary

We have been able to run full scale simulations of EMIC waves with realistic particle distributions. The most important results of our study are:

1. While an exact comparison between observed and simulated spectra is not possible given the data available, we do find significant similarities between the two, at least at one location within the region of largest wave growth (Subsection 5.7).
2. The plasmopause is not a preferred region for EMIC wave growth, though waves can grow in that region (Subsection 5.1). The density gradient within the plasmopause does, however, affect the orientation of wave fronts and wave vector both within the plasmopause and in adjacent regions.

3. There is a preference for EMIC waves to be driven in the He+ band within the plasmasphere (or high density region), although they can also grow in the plasmatrough (low density region). If present, H+ band waves are more likely to grow in the plasmatrough (Subsection 5.3).

4. This fact, plus the L dependence of the frequency and possible time evolution toward lower frequency waves can be explained by a simple model (Subsection 5.3).

5. Large O+ concentration limits the frequency range of, or even totally quenches, EMIC waves. This is more likely to occur in the plasmatrough at solar maximum (Subsection 5.4).

6. Large O+ concentration can significantly affect the H+ cutoff frequency, and hence the width in frequency of the stop band above Ω_{cHe} .

7. The finite temperature of the ring current H+ can make cold plasma theory insufficient for describing EMIC wave surfaces (Subsection 5.5).

Acknowledgments. We thank Alexa Halford, Jay Johnson and Jacob Bortnik for helpful discussions. Work at Dartmouth was supported by NASA grants NNX10AQ60G, NNX13AD65G, and NNX08AM58G. Work at Los Alamos was conducted under the auspices of the United States Department of Energy with partial support from NASA grants NNH10AP09I and NNH13AW83I, and NSF grant AGR1203460. Work at Newcastle Australia was supported by ARC grant DP0772504. We thank Howard Singer for supplying GOES magnetometer data. Numerical data shown in this paper is available from the lead author upon request.

References

- Anderson, B. J., and D. C. Hamilton (1993), Electromagnetic ion-cyclotron waves stimulated by modest magnetospheric compressions, *J. Geophys. Res.*, *98*(A7), 11,369–11,382.
- Anderson, B. J., R. E. Erlandson, and L. J. Zanetti (1992a), A statistical study of PC 1-2 magnetic pulsations in the equatorial magnetosphere. 1. Equatorial occurrence distributions, *J. Geophys. Res.*, *97*(A3), 3075–3088, doi:10.1029/91ja02706.
- Anderson, B. J., R. E. Erlandson, and L. J. Zanetti (1992b), A statistical study of pc 1-2 magnetic pulsations in the equatorial magnetosphere .2. wave properties, *J. Geophys. Res.*, *97*(A3), 3089–3101, doi:10.1029/91ja02697.
- Andre, M. (1985), Dispersion surfaces, *Journal of Plasma Physics*, *33*(FEB), 1–19.
- Arfken, G. (1970), *Mathematical Methods for Physicists*, 2nd ed., Academic Press, New York.
- Blum, L. W., E. A. MacDonald, S. P. Gary, M. F. Thomsen, and H. E. Spence (2009), Ion observations from geosynchronous orbit as a proxy for ion cyclotron wave growth during storm times, *J. Geophys. Res.*, *114*, doi:10.1029/2009ja014396.
- Bortnik, J., N. Omidi, L. Chen, R. M. Thorne, and R. B. Horne (2011), Saturation characteristics of electromagnetic ion cyclotron waves, *J. Geophys. Res.*, *116*, a09219, doi:10.1029/2011ja016638.
- Chappell, C. R., M. M. Huddleston, T. E. Moore, B. L. Giles, and D. C. Delcourt (2008), Observations of the warm plasma cloak and an explanation of its formation in the magnetosphere, *J. Geophys. Res.*, *113*(A9), a09206, doi:10.1029/2007ja012945.

Chen, L., R. M. Thorne, and R. B. Horne (2009), Simulation of EMIC wave excitation in a model magnetosphere including structured high-density plumes, *J. Geophys. Res.*, *114*, a07221, doi:10.1029/2009ja014204.

Chen, L., R. M. Thorne, V. K. Jordanova, C.-P. Wang, M. Gkioulidou, L. Lyons, and R. B. Horne (2010), Global simulation of EMIC wave excitation during the 21 April 2001 storm from coupled RCM-RAM-HOTRAY modeling, *J. Geophys. Res.*, *115*, a07209, doi:10.1029/2009ja015075.

Chen, L., R. M. Thorne, and J. Bortnik (2011), The controlling effect of ion temperature on emic wave excitation and scattering, *Geophys. Res. Lett.*, *38*, 116109, doi:10.1029/2011gl048653.

Chen, L., V. K. Jordanova, M. Spasojevic, R. M. Thorne, and R. B. Horne (2014), Electromagnetic ion cyclotron wave modeling during the Geospace Environment Modeling challenge event, *J. Geophys. Res.*, *119*.

de Soria-Santacruz, M., M. Spasojevic, and L. Chen (2013), EMIC waves growth and guiding in the presence of cold plasma density irregularities, *Geophys. Res. Lett.*, *40*(10), 1940–1944, doi:10.1002/grl.50484.

Denton, R. E., and Y. Hu (2010), Two-dimensional hybrid simulation of the growth, effects, and distribution of magnetospheric electromagnetic ion cyclotron waves, Abstract SM21D-03, in *2010 Fall Meeting, AGU, San Francisco, Calif., 13-17 Dec.*

Denton, R. E., M. K. Hudson, and I. Roth (1992), Loss-cone-driven ion cyclotron waves in the magnetosphere, *Journal of Geophysical Research*, *97*(A8), 12,093–12,103.

Denton, R. E., M. K. Hudson, S. A. Fuselier, and B. J. Anderson (1993), Electromagnetic ion cyclotron waves in the plasma depletion layer, *Journal of Geophysical Research*,

- 912 98(A8), 13,477–13,490.
- 913 Denton, R. E., B. J. Anderson, S. P. Gary, and S. A. Fuselier (1994), Bounded anisotropy
914 fluid model for ion temperatures, *J. Geophys. Res.*, 99(A6).
- 915 Denton, R. E., M. F. Thomsen, K. Takahashi, R. R. Anderson, and H. J. Singer (2011),
916 Solar cycle dependence of bulk ion composition at geosynchronous orbit, *J. Geophys.*
917 *Res.*, 116, a03212, doi:10.1029/2010ja016027.
- 918 Denton, R. E., K. Takahashi, and M. F. Thomsen (2012), O⁺ concentration at geosyn-
919 chronous orbit, Abstract SA31C-01, in *2012 Fall Meeting, AGU, San Francisco, Calif.*,
920 3-7 Dec.
- 921 Denton, R. E., K. Takahashi, M. Thomsen, J. E. Borovsky, H. J. Singer, Y. Wang,
922 J. Goldstein, P. C. Brandt, and B. W. Reinisch (2014), Evolution of O⁺ concentra-
923 tion at geostationary orbit during storm and quiet events, *J. Geophys. Res.*, 119(8),
924 6417, doi:10.1002/2014JA019888.
- 925 Fraser, B. J., and T. S. Nguyen (2001), Is the plasmopause a preferred source region of
926 electromagnetic ion cyclotron waves in the magnetosphere?, *J. Atmos. Sol.-Terr. Phys.*,
927 63(11).
- 928 Fraser, B. J., H. J. Singer, M. L. Adrian, and D. L. Gallagher (2005), The relationship
929 between plasma density structure and emic waves at geosynchronous orbit, in *Inner*
930 *Magnetosphere Interactions: New Perspectives from Imaging, Geophys. Monog. Ser.*,
931 *vol. 159*, edited by J. L. Burch, M. Schulz, and H. Spence, pp. 55 – 70, AGU, Washing-
932 ton, D. C.
- 933 Gamayunov, K. V., and G. V. Khazanov (2008), Crucial role of ring current H⁺ in
934 electromagnetic ion cyclotron wave dispersion relation: Results from global simulations,

J. Geophys. Res., *113*(A11), doi:10.1029/2008JA013494.

Gamayunov, K. V., G. V. Khazanov, M. W. Liemohn, M. C. Fok, and A. J. Ridley (2009), Self-consistent model of magnetospheric electric field, ring current, plasmasphere, and electromagnetic ion cyclotron waves: Initial results, *J. Geophys. Res.*, *114*, doi:10.1029/2008JA013597.

Gary, S. P., and M. A. Lee (1994), The ion-cyclotron anisotropy instability and the inverse correlation between proton anisotropy and proton-beta, *J. Geophys. Res.*, *99*(A6), 11,297–11,301.

Gary, S. P., M. B. Moldwin, M. F. Thomsen, D. Winske, and D. J. McComas (1994a), Hot proton anisotropies and cool proton temperatures in the outer magnetosphere, *J. Geophys. Res.*, *99*(A12), 23,603–23,615.

Gary, S. P., P. D. Convery, R. E. Denton, S. A. Fuselier, and B. J. Anderson (1994b), Proton and helium cyclotron anisotropy instability thresholds in the magnetosheath, *J. Geophys. Res.*, *99*(A4).

Gary, S. P., B. J. Anderson, R. E. Denton, S. A. Fuselier, and M. E. McKean (1994c), A limited closure relation for anisotropic plasmas from the earth's magnetosheath, *Phys. Plasmas*, *1*(5).

Gary, S. P., M. F. Thomsen, L. Yin, and D. Winske (1995), Electromagnetic proton cyclotron instability: Interactions with magnetospheric protons, *J. Geophys. Res.*, *100*(A11), 21,961–21,972.

Halford, A. J., B. J. Fraser, and S. K. Morley (2010), Emic wave activity during geomagnetic storm and nonstorm periods: Ceres results, *J. Geophys. Res.*, *115*, a12248, doi:10.1029/2010ja015716.

- 958 Halford, A. J., B. J. Fraser, and S. K. Morley (2014), EMIC waves and plasmaspheric and
959 plume density: CRRES results, *J. Geophys. Res.*, *119*.
- 960 Horne, R. B., and R. M. Thorne (1997), Wave heating of He⁺ by electromagnetic ion
961 cyclotron waves in the magnetosphere: Heating near the H⁺-He⁺ bi-ion resonance
962 frequency, *J. Geophys. Res.*, *102*(A6), 11,457–11,471, doi:10.1029/97ja00749.
- 963 Hu, Y., and R. E. Denton (2009), Two-dimensional hybrid code simulation of electro-
964 magnetic ion cyclotron waves in a dipole magnetic field, *J. Geophys. Res.*, *114*, doi:
965 10.1029/2009ja014570.
- 966 Hu, Y., R. E. Denton, and J. R. Johnson (2010), Two-dimensional hybrid code simulation
967 of electromagnetic ion cyclotron waves of multi-ion plasmas in a dipole magnetic field,
968 *J. Geophys. Res.*, *115*, a09218, doi:10.1029/2009ja015158.
- 969 Jordanova, V. K., L. M. Kistler, J. U. Kozyra, G. V. Khazanov, and A. F. Nagy
970 (1996), Collisional losses of ring current ions, *J. Geophys. Res.*, *101*(A1), 111–126,
971 doi:10.1029/95ja02000.
- 972 Jordanova, V. K., C. J. Farrugia, R. M. Thorne, G. V. Khazanov, G. D. Reeves, and M. F.
973 Thomsen (2001a), Modeling ring current proton precipitation by electromagnetic ion
974 cyclotron waves during the May 14-16, 1997, storm, *J. Geophys. Res.*, *106*(A1), 7–22,
975 doi:10.1029/2000ja002008.
- 976 Jordanova, V. K., C. J. Farrugia, J. F. Fennell, and J. D. Scudder (2001b), Ground dis-
977 turbances of the ring, magnetopause, and tail currents on the day the solar wind almost
978 disappeared, *J. Geophys. Res.*, *106*(A11), 25,529–25,540, doi:10.1029/2000ja000251.
- 979 Jordanova, V. K., Y. S. Miyoshi, S. Zaharia, M. F. Thomsen, G. D. Reeves, D. S. Evans,
980 C. G. Mouikis, and J. F. Fennell (2006), Kinetic simulations of ring current evolu-

tion during the Geospace Environment Modeling challenge events, *J. Geophys. Res.*,
111(A11), a11s10, doi:10.1029/2006ja011644.

Jordanova, V. K., J. Albert, and Y. Miyoshi (2008), Relativistic electron precipitation
by EMIC waves from self-consistent global simulations, *J. Geophys. Res.*, 113, a00a10,
doi:10.1029/2008ja013239.

Jordanova, V. K., D. T. Welling, S. G. Zaharia, L. Chen, and R. M. Thorne (2012),
Modeling ring current ion and electron dynamics and plasma instabilities during a high-
speed stream driven storm, *J. Geophys. Res.*, 117, a00l08, doi:10.1029/2011ja017433.

Kennel, C. F., and H. E. Petschek (1966), Limit on stably trapped particle fluxes, *Journal
of Geophysical Research*, 71(1), 1.

Khazanov, G. V., K. V. Gamayunov, D. L. Gallagher, and J. U. Kozyra (2007), Reply to
comment by R. M. Thorne and R. B. Horne Khazanov et al. 2002 and Khazanov et al.
2006, *J. Geophys. Res.*, 112(A12), doi:10.1029/2007ja012463.

Lee, J. H., and V. Angelopoulos (2014), On the presence and properties of cold ions
near earth's equatorial magnetosphere, *J. Geophys. Res.*, 119(3), 1749–1770, doi:
10.1002/2013ja019305.

Meredith, N. P., R. M. Thorne, R. B. Horne, D. Summers, B. J. Fraser, and R. R.
Anderson (2003), Statistical analysis of relativistic electron energies for cyclotron res-
onance with EMIC waves observed on CRRES, *J. Geophys. Res.*, 108(A6), 1250, doi:
10.1029/2002ja009700.

Millan, R. M., and R. M. Thorne (2007), Review of radiation belt relativistic electron
losses, *J. Atmos. Sol.-Terr. Phys.*, 69(3), 362–377, doi:10.1016/j.jastp.2006.06.019.

- 1003 Omid, N., R. M. Thorne, and J. Bortnik (2010), Nonlinear evolution of EMIC waves
1004 in a uniform magnetic field: 1. Hybrid simulations, *J. Geophys. Res.*, *115*, a12241,
1005 doi:10.1029/2010ja015607.
- 1006 Omid, N., R. Thorne, and J. Bortnik (2011), Hybrid simulations of EMIC waves in a
1007 dipolar magnetic field, *J. Geophys. Res.*, *116*, a09231, doi:10.1029/2011ja016511.
- 1008 Omid, N., J. Bortnik, R. Thorne, and L. Chen (2013), Impact of cold O+ ions on
1009 the generation and evolution of EMIC waves, *J. Geophys. Res.*, *118*(1), 434–445, doi:
1010 10.1029/2012ja018319.
- 1011 Rasmussen, C. E., S. M. Guiter, and S. G. Thomas (1993), A 2-dimensional model
1012 of the plasmasphere: Refilling time constants, *Planet Space Sci.*, *41*(1), 35–43, doi:
1013 10.1016/0032-0633(93)90015-t.
- 1014 Ronnmark, K. (1982), Waves in homogeneous, anisotropic, multicomponent plasmas,
1015 *Tech. Rep. Kiruna Geophys. Inst. Rep. 179, 56 pp.*, Swedish Institute of Space Physics,
1016 Univ. of Umea, Sweden.
- 1017 Selesnick, R. S. (2006), Source and loss rates of radiation belt relativistic electrons during
1018 magnetic storms, *J. Geophys. Res.*, *111*(A4), a04210, doi:10.1029/2005ja011473.
- 1019 Shoji, M., and Y. Omura (2011), Simulation of electromagnetic ion cyclotron triggered
1020 emissions in the earth’s inner magnetosphere, *J. Geophys. Res.*, *116*, a05212, doi:
1021 10.1029/2010ja016351.
- 1022 Shoji, M., Y. Omura, B. Grison, J. Pickett, I. Dandouras, and M. Engebretson (2011),
1023 Electromagnetic ion cyclotron waves in the helium branch induced by multiple elec-
1024 tromagnetic ion cyclotron triggered emissions, *Geophys. Res. Lett.*, *38*, 117102, doi:
1025 10.1029/2011gl048427.

- Shprits, Y. Y., D. A. Subbotin, N. P. Meredith, and S. R. Elkington (2008), Review of modeling of losses and sources of relativistic electrons in the outer radiation belt. ii: Local acceleration and loss, *J. Atmos. Sol.-Terr. Phys.*, *70*(14), 1694–1713, doi:10.1016/j.jastp.2008.06.014.
- Spasojevic, M., H. U. Frey, M. F. Thomsen, S. A. Fuselier, S. P. Gary, B. R. Sandel, and U. S. Inan (2004), The link between a detached subauroral proton arc and a plasmaspheric plume, *Geophys. Res. Lett.*, *31*(4), doi:10.1029/2003gl018389.
- Swanson, D. G. (2003), *Plasma Waves*, 2nd ed., Institute of Physics Publishing, Bristol and Philadelphia.
- Takahashi, K., R. E. Denton, R. R. Anderson, and W. J. Hughes (2006), Mass density inferred from toroidal wave frequencies and its comparison to electron density, *J. Geophys. Res.*, *111*(A1), A01201, doi:10.1029/2005JA011286.
- Takahashi, K., S. Ohtani, R. E. Denton, W. J. Hughes, and R. R. Anderson (2008), Ion composition in the plasma trough and plasma plume derived from a Combined Release and Radiation Effects Satellite magnetoseismic study, *J. Geophys. Res.*, *113*(A12), A12203, doi:10.1029/2008JA013248.
- Thorne, R. M., and R. B. Horne (1992), The contribution of ion-cyclotron waves to electron heating and SAR-arc excitation near the storm-time plasmopause, *Geophys. Res. Lett.*, *19*(4), 417–420, doi:10.1029/92gl00089.
- Thorne, R. M., and R. B. Horne (1997), Modulation of electromagnetic ion cyclotron instability due to interaction with ring current O+ during magnetic storms, *J. Geophys. Res.*, *102*(A7), 14,155–14,163, doi:10.1029/96ja04019.

- 1048 Thorne, R. M., and R. B. Horne (2007), Khazanov et al. 2002 and Khazanov et al. 2006,
1049 *J. Geophys. Res.*, *112*(A12), a12214, doi:10.1029/2007ja012268.
- 1050 Tsyganenko, N. A., and M. I. Sitnov (2005), Modeling the dynamics of the inner
1051 magnetosphere during strong geomagnetic storms, *J. Geophys. Res.*, *110*(A3), doi:
1052 10.1029/2004ja010798.
- 1053 Uberoi, C. (1973), Crossover frequencies in multicomponent plasma, *Phys. Fluids*, *16*(5),
1054 704–705, doi:10.1063/1.1694411.
- 1055 Usanova, M. E., F. Darrouzet, I. R. Mann, and J. Bortnik (2013), Statistical analysis
1056 of EMIC waves in plasmaspheric plumes from Cluster observations, *J. Geophys. Res.*,
1057 *118*(8), 4946–4951, doi:10.1002/jgra.50464.
- 1058 Weimer, D. R. (2001), An improved model of ionospheric electric potentials including sub-
1059 storm perturbations and application to the geospace environment modeling november
1060 24, 1996, event, *J. Geophys. Res.*, *106*(A1), 407–416, doi:10.1029/2000ja000604.
- 1061 Yahnin, A. G., and T. A. Yahnina (2007), Energetic proton precipitation re-
1062 lated to ion-cyclotron waves, *J. Atmos. Sol.-Terr. Phys.*, *69*(14), 1690–1706, doi:
1063 10.1016/j.jastp.2007.02.010.
- 1064 Yahnina, T. A., et al. (2003), Energetic particle counterparts for geomagnetic pulsations
1065 of Pc1 and IPDP types, *Ann. Geophys.*, *21*(12), 2281–2292.
- 1066 Young, D. T., H. Balsiger, and J. Geiss (1982), Correlations of magnetospheric ion com-
1067 position with geomagnetic and solar-activity, *J. Geophys. Res.*, *87*(NA11), 9077–9096.
- 1068 Zaharia, S., V. K. Jordanova, D. Welling, and G. Toth (2010), Self-consistent inner mag-
1069 netosphere simulation driven by a global MHD model, *J. Geophys. Res.*, *115*, doi:
1070 10.1029/2010ja015915.

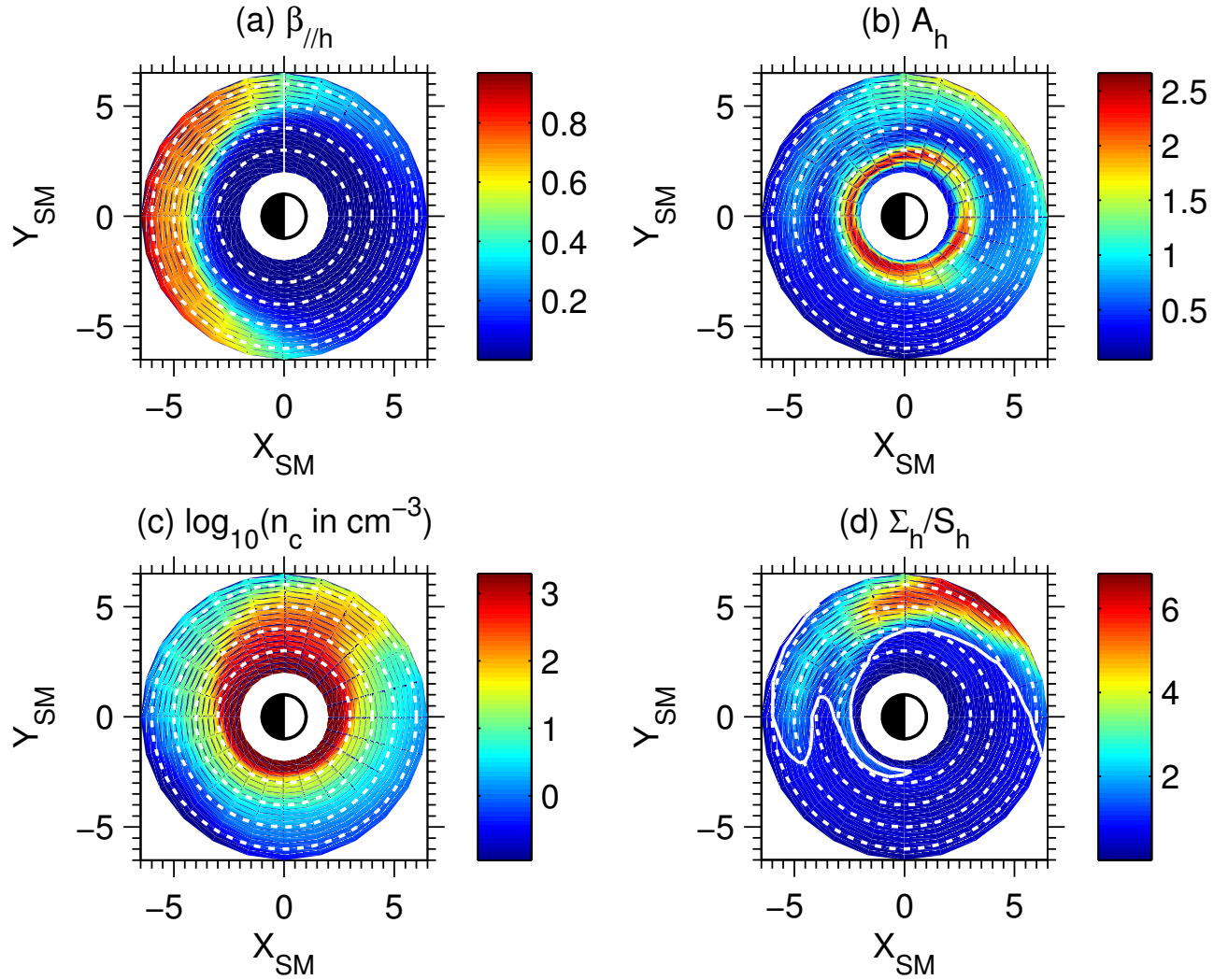


Figure 1. (a) Ring current H+ $\beta_{\parallel h}$, (b) ring current H+ anisotropy A_h , (c) base 10 logarithm of the cold density n_c in cm^{-3} , and (d) the ratio of the EMIC instability parameter Σ_h to the threshold value S_h . The white solid line in (a) is along $\text{MLT} = 18$, while the white solid curve in (d) is $\Sigma_h/S_h = 1$. The dotted white circles are at $L = 3, 4, 5$, and 6 .

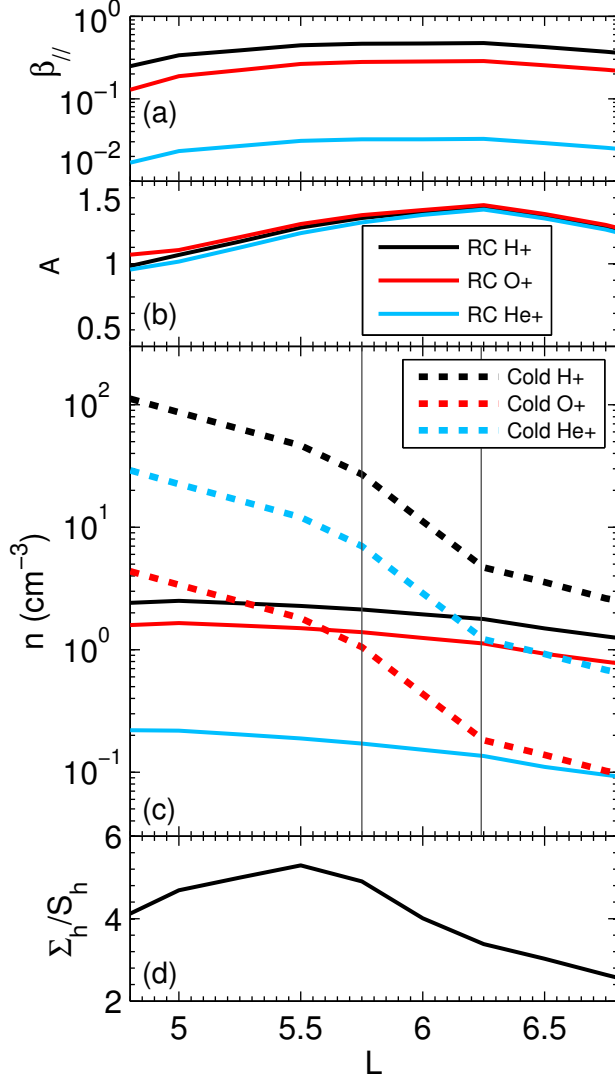


Figure 2. (a) Ring current $\beta_{\parallel s}$, (b) ring current anisotropy A_s , (c) density in cm^{-3} , and (d) the ratio of the EMIC instability parameter Σ_h to the threshold value S_h , for species s . The solid curves show ring current quantities for H+ in black, He+ in blue, and O+ in red. The dotted curves show the cold density using the same colors for the constant composition model described in the text. The two vertical gray lines in panel (c) roughly delineate the plasmapause.

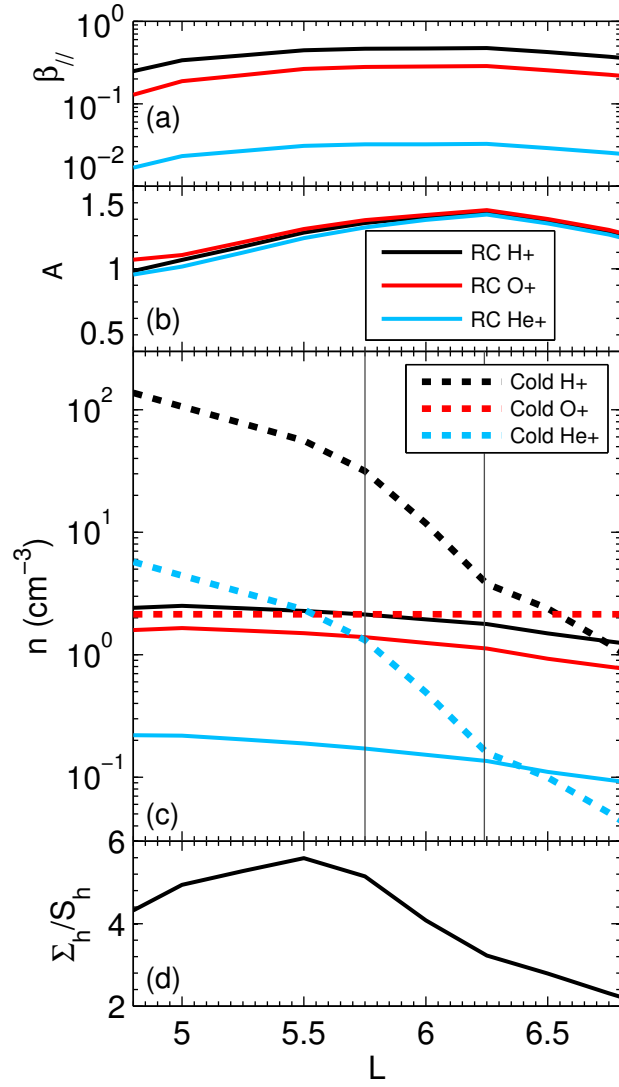


Figure 3. Same as Figure 2, except for the variable composition model described in the text.

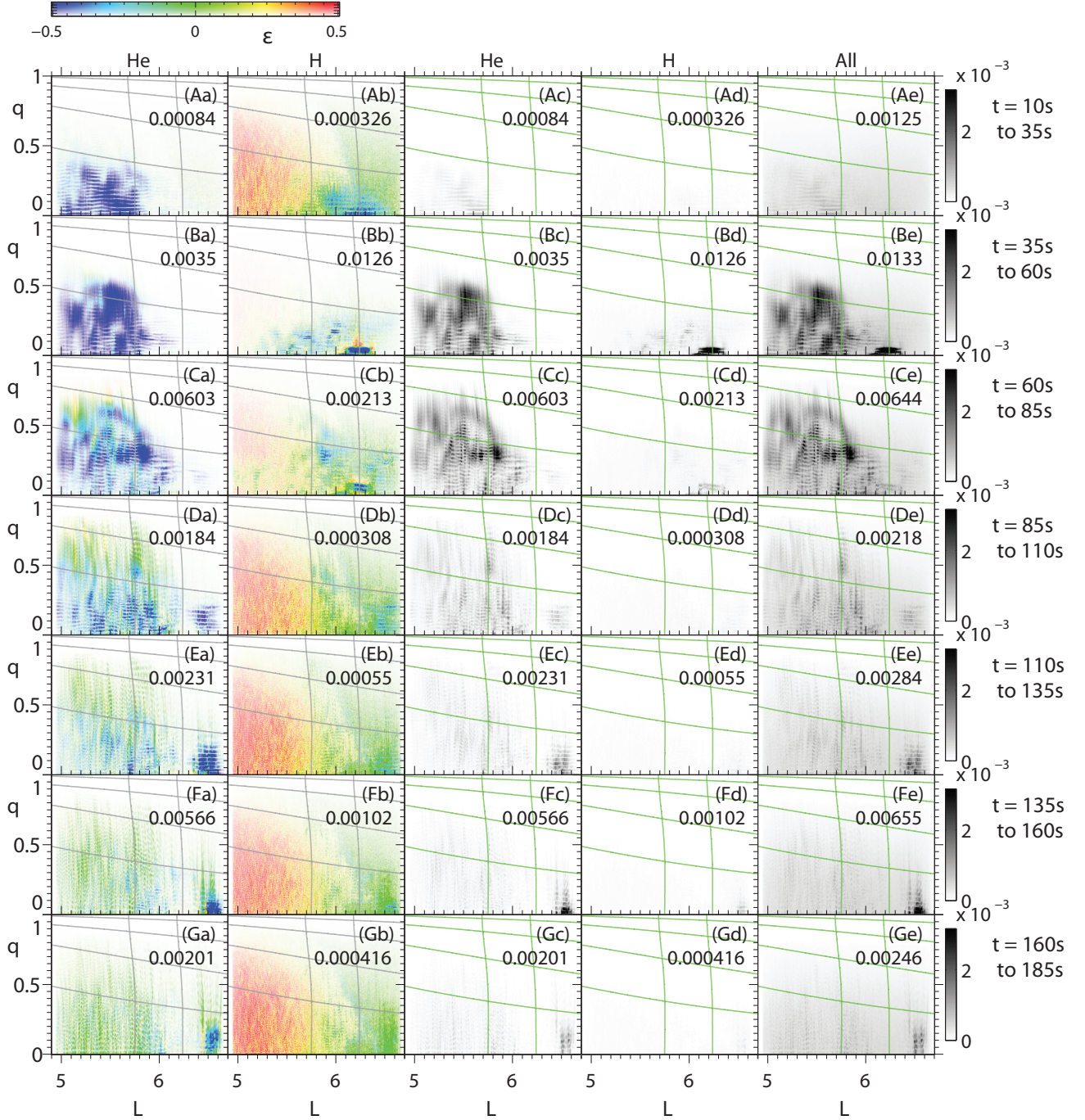


Figure 4. For the time spans indicated at the right side of the figure (rows “A”, “B”, etc), wave power normalized to the local magnetic field versus L shell on the horizontal axis and the parallel coordinate q on the vertical axis. The right three columns (“c”, “d”, and “e”) show wave power using the same constant color scale (at right of column “e”) for the He⁺ band, the H⁺ band, and all frequencies, respectively. Columns “a” and “b” also show the wave power in the He⁺ and H⁺ bands, respectively, but in these panels saturated color corresponds to maximum wave power in that panel and the hue of the color corresponds to the ellipticity using the scale at the top left of the figure. The maximum wave power in each panel is listed under the panel label. The roughly vertical curves in each panel are flux surfaces delineating the plasmapause as in Figure 2 and the roughly horizontal curves show MLAT values of 10° , 20° , 30° , and 40° .

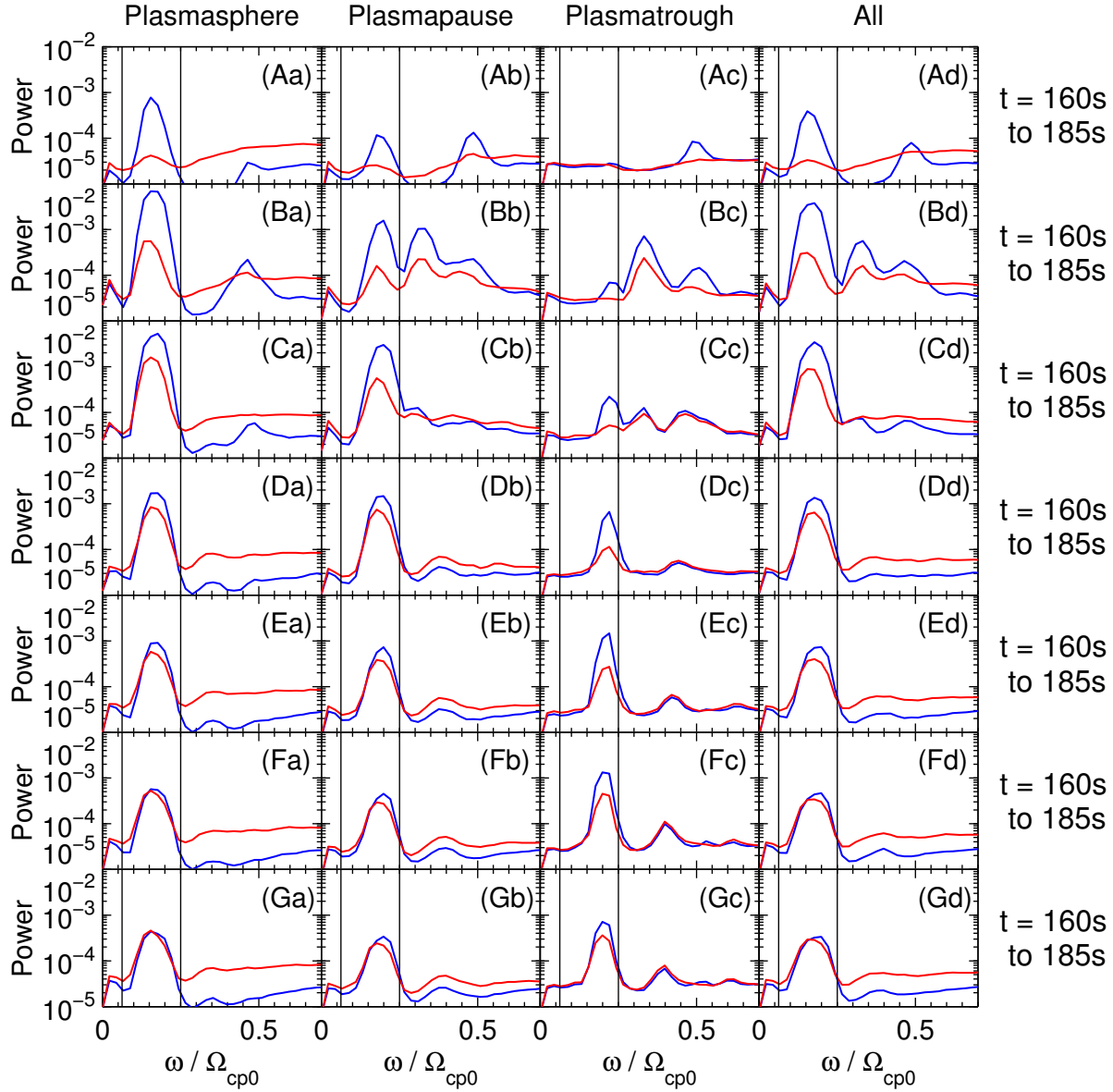


Figure 5. Average wave power normalized to the local magnetic field per unit ω/Ω_{cp0} versus ω/Ω_{cp0} for the time intervals indicated at the right side of each row (labeled “A”, “B”, etc). The blue curves are left hand polarized wave power, while the red curves are right hand polarized wave power. The left and right vertical gray lines in each panel are respectively at the O⁺ and He⁺ gyrofrequencies. The panels in the first column (labeled with “a”) show the wave power in the plasmasphere; the panels in the second column (labeled with “b”) show the wave power in the plasmapause; and the panels in the third column (labeled with “c”) show the wave power in the plasmatrough. The fourth column (labeled with “d”) shows the wave power averaged over the entire simulation domain.

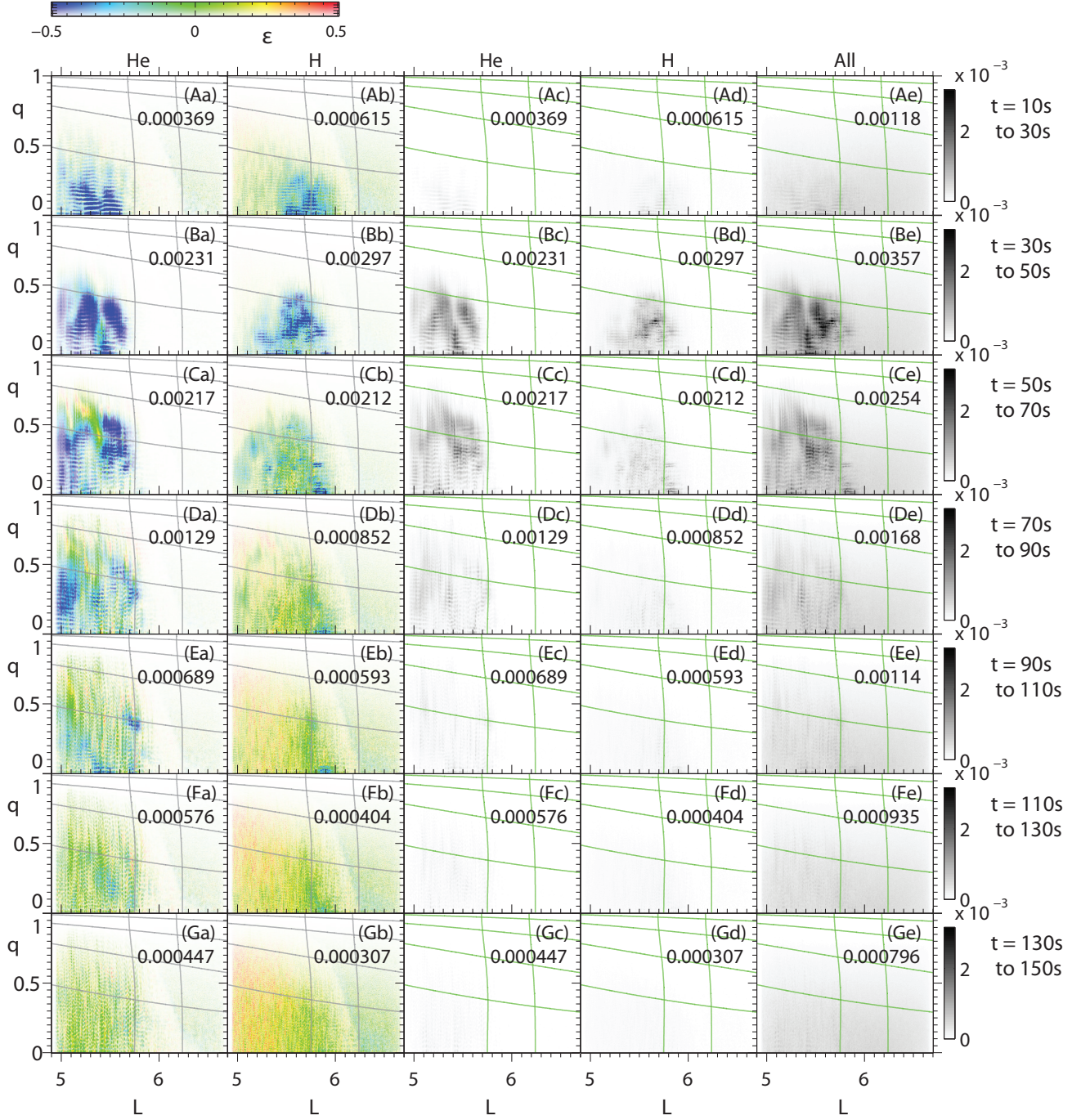


Figure 6. Same as Figure 4, but for the variable cold composition model with low He+ concentration and low O+ concentration in the plasmasphere, but high O+ concentration in the plasmatrrough.

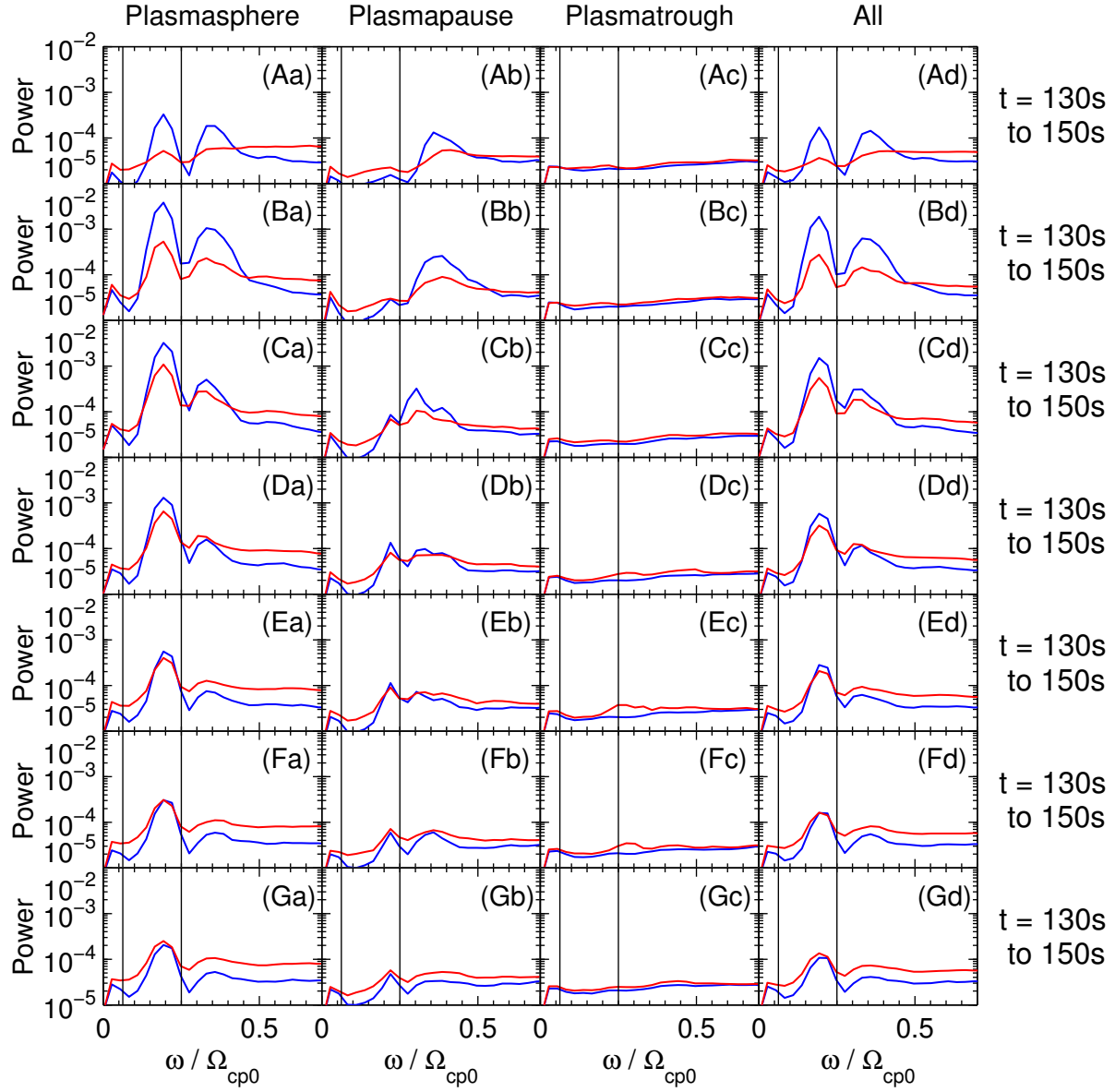


Figure 7. Same as Figure 5, but for the variable cold composition model with low He+ concentration and low O+ concentration in the plasmasphere, but high O+ concentration in the plasmatrough.

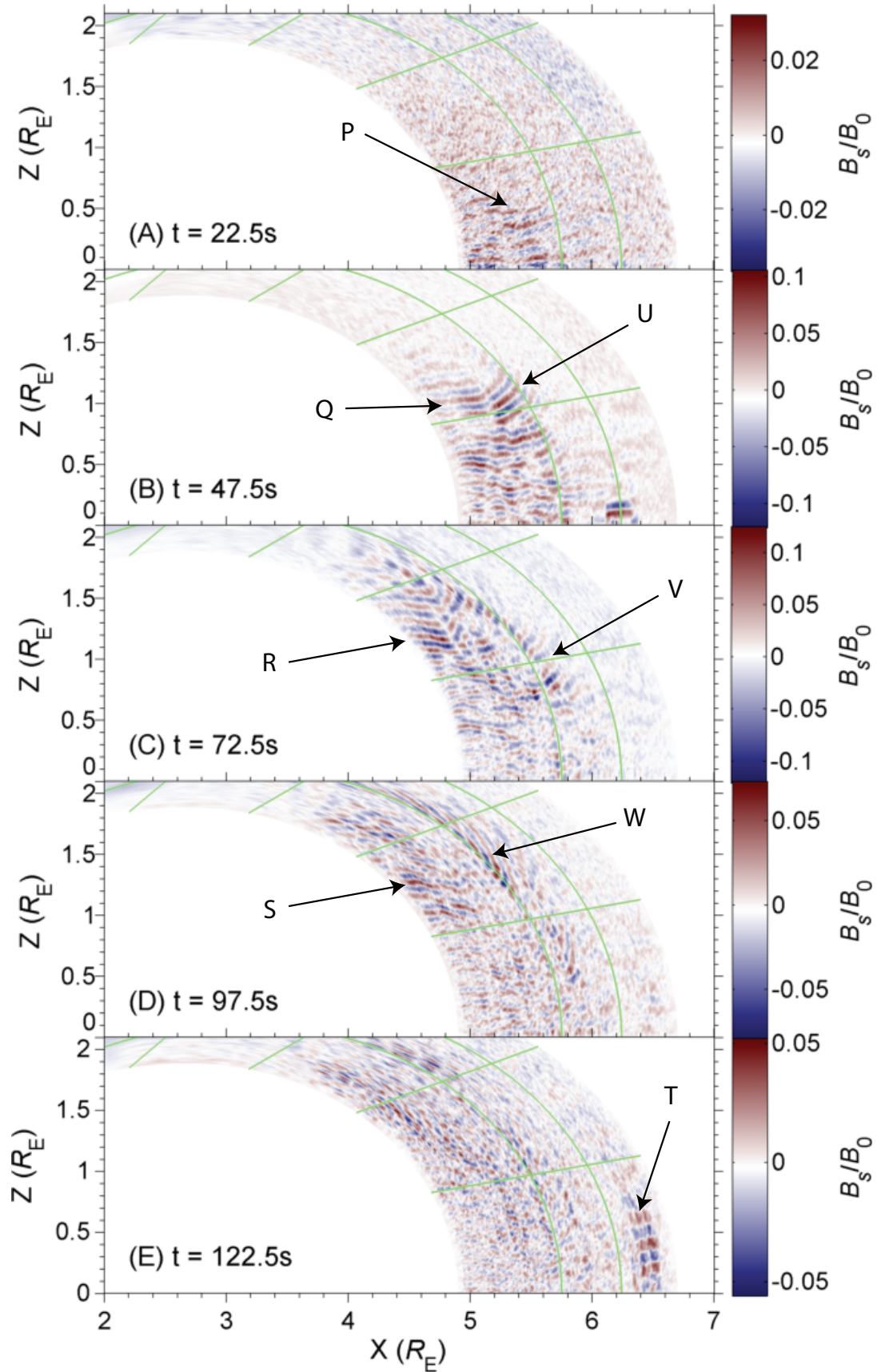


Figure 8. Out of plane (“s”) component of the wave magnetic field, B_s , in the meridional plane of the simulation normalized to the equatorial magnetic field at the central L shell, B_0 ; Z is the coordinate along the dipole axis while X is the radius in cylindrical coordinates. Each panel shows B_s/B_0 at the central time of one of the first five time intervals plotted in Figure 4. The green curves that intersect $Z = 0$ are magnetic flux surfaces at the plasmopause boundaries shown in Figure 2. The green curves roughly normal to these are at MLAT = 10° , D R A F T

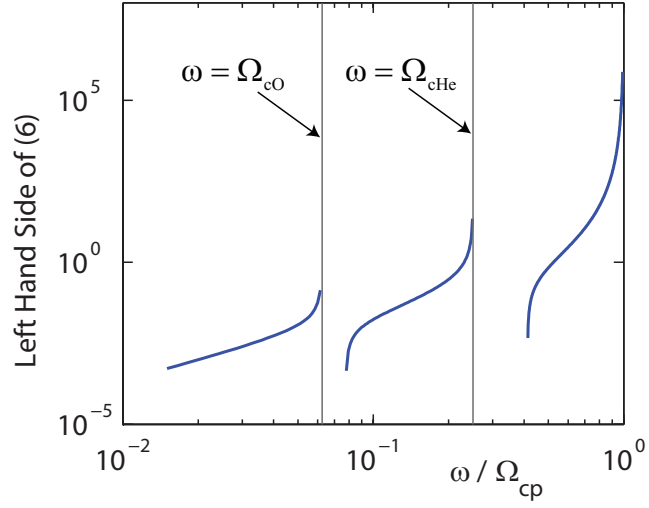


Figure 9. The left-hand side of equation (6) versus $\bar{\omega} \equiv \omega/\Omega_{cp}$ for $\eta_H = 0.77$, $\eta_{He} = 0.20$, and $\eta_O = 0.03$.

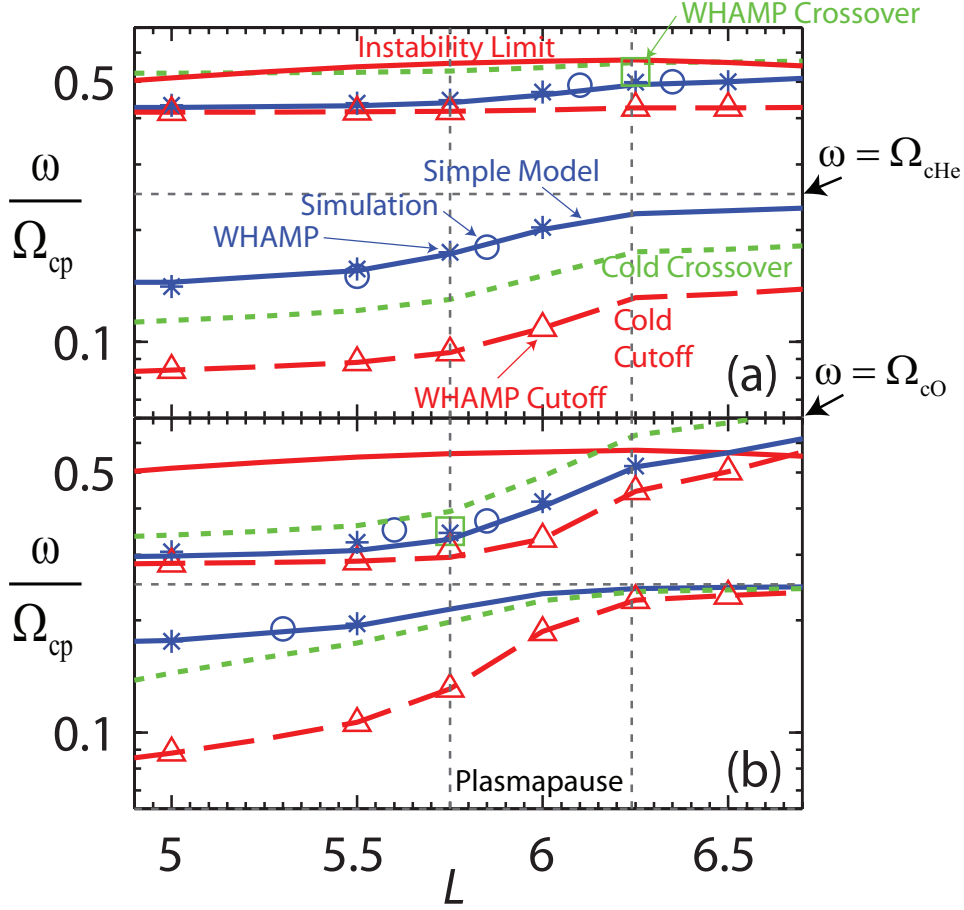


Figure 10. For (a) the constant cold composition model, and (b) the variable cold composition model, normalized frequency ω/Ω_{cp} plotted using a log scale versus L shell. The solid blue curves are the unstable frequency based on (6); the blue asterisks show the frequency of maximum growth rate predicted by WHAMP; the blue circles show the frequency of waves observed in our simulations; the red solid curve shows the maximum possible frequency based on (7); the dashed red curves show the cutoff frequency corresponding to $k_{\parallel} = 0$ for left hand polarized waves; the upward pointing red triangles show the cutoff frequency determined from WHAMP; the dotted green curves show the cold plasma crossover frequency; and the green squares show the crossover frequency found from WHAMP. The dotted vertical gray lines delineate the plasmapause while the dotted horizontal gray line corresponds to $\omega = \Omega_{cHe}$ and the bottom of each panel is at $\omega = \Omega_{cO}$.

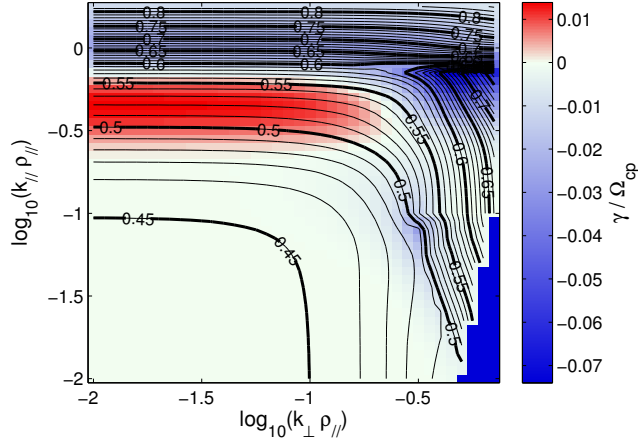


Figure 11. Based on calculations by WHAMP for the H+ mode at the outer edge of the plasmopause in the constant cold composition model, black contour lines for ω/Ω_{cp} and color for normalized growth rate γ/Ω_{cp} versus $\log_{10}(k_{\perp}\rho_{\perp})$ and $\log_{10}(k_{\parallel}\rho_{\parallel})$, where ρ_{\parallel} is the gyroradius defined using the parallel thermal velocity.

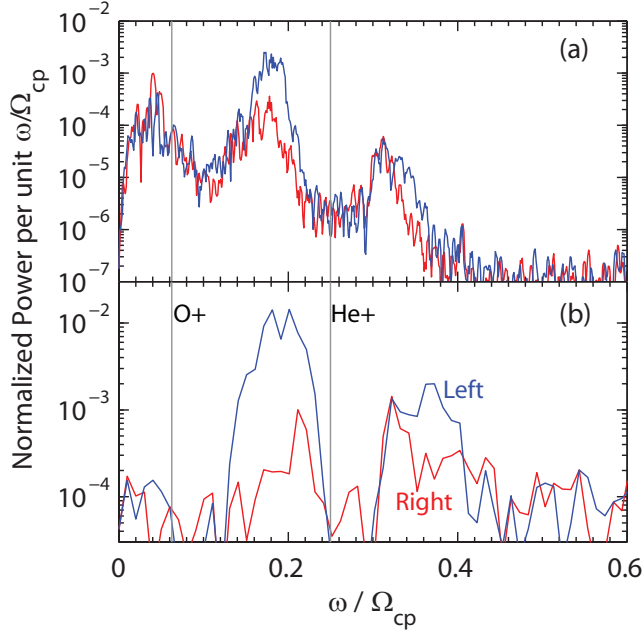
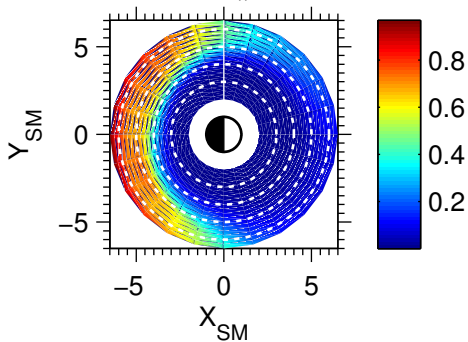
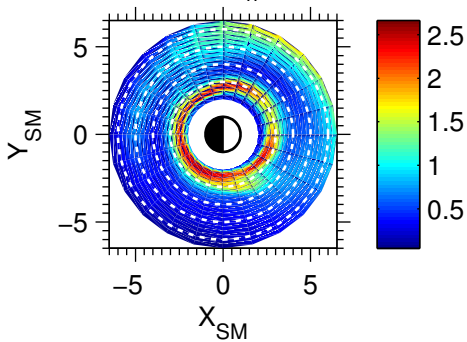
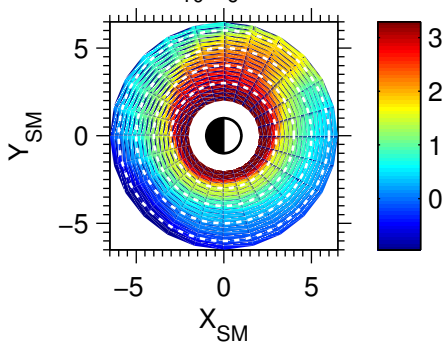
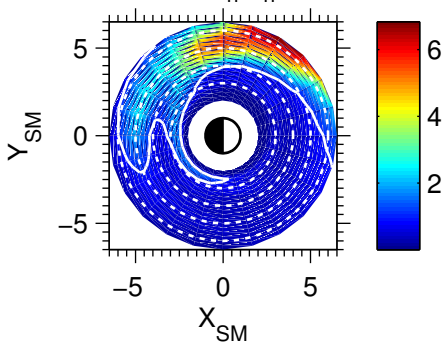
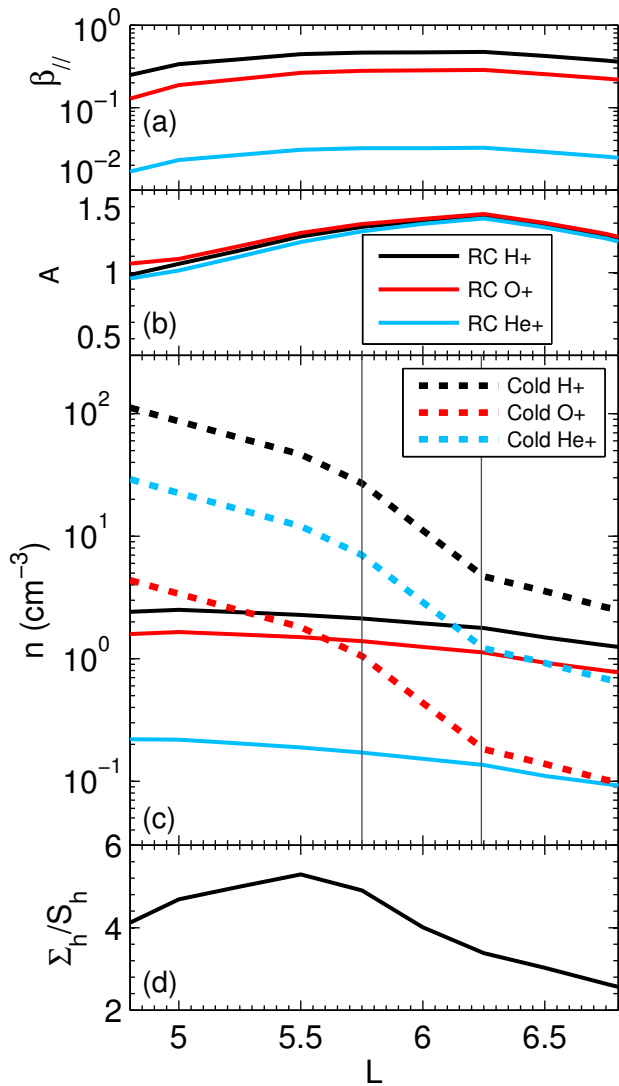
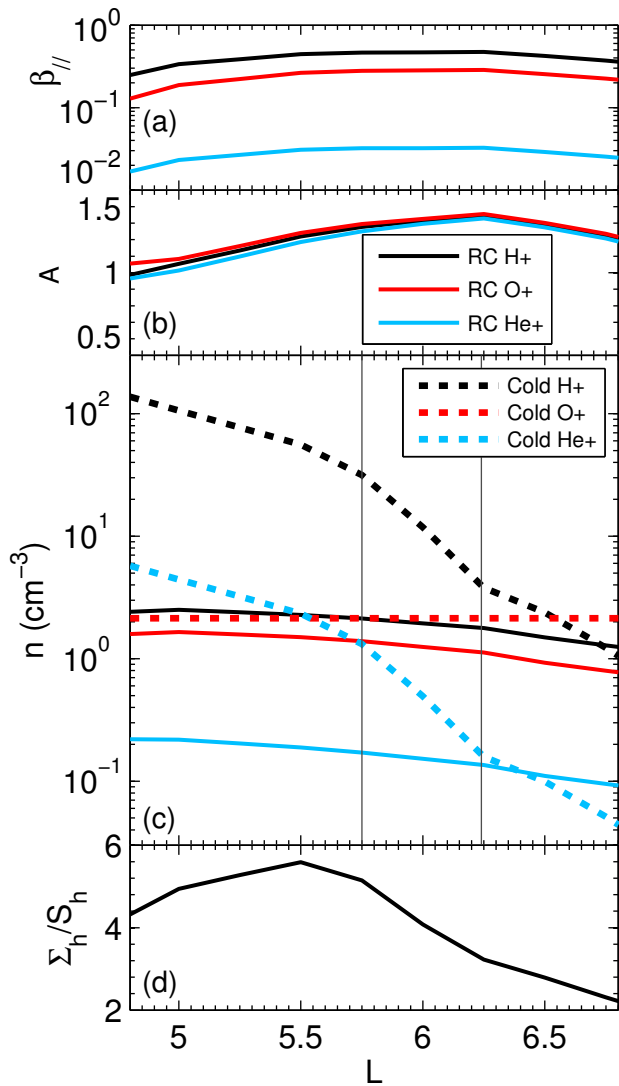
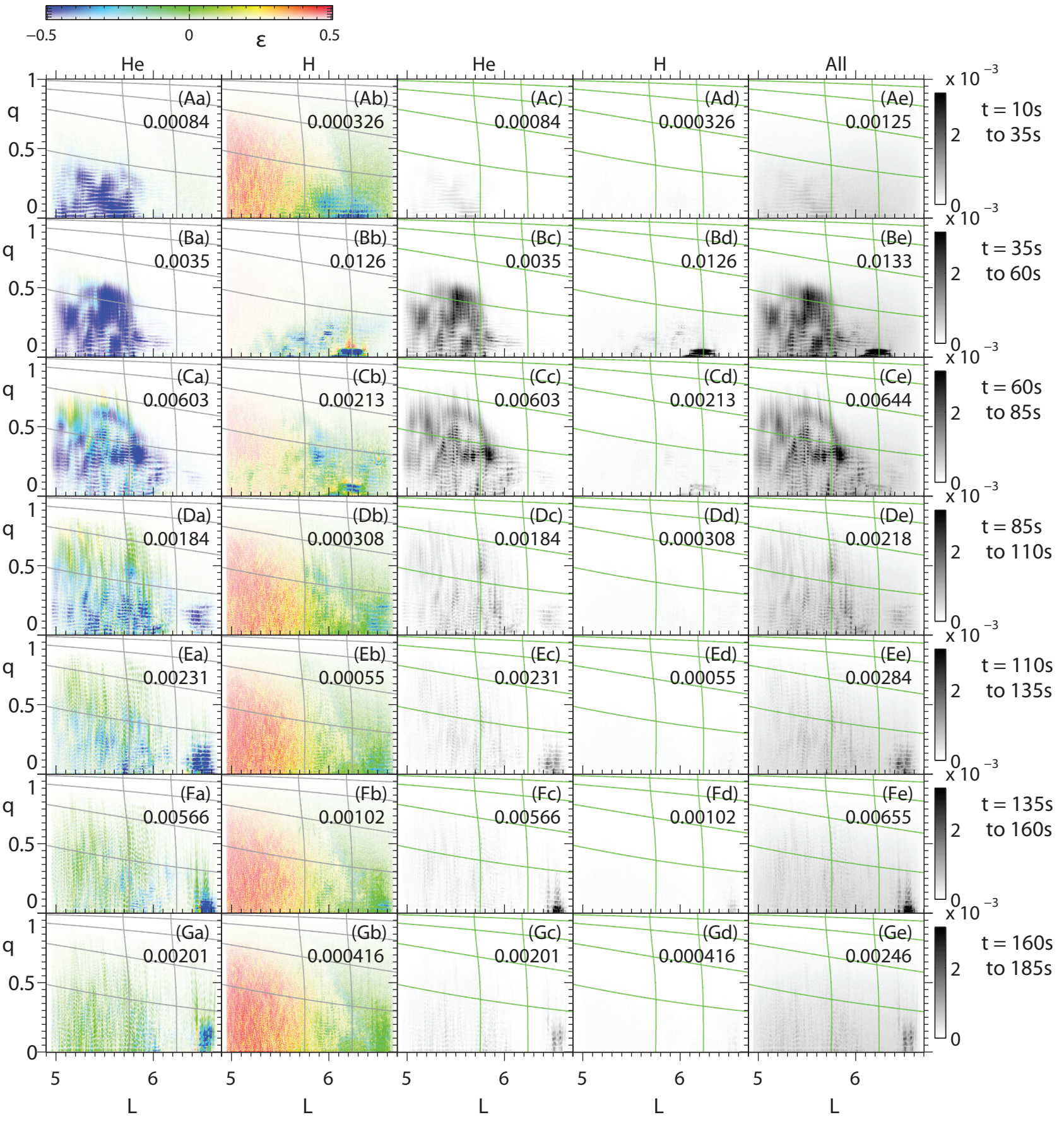


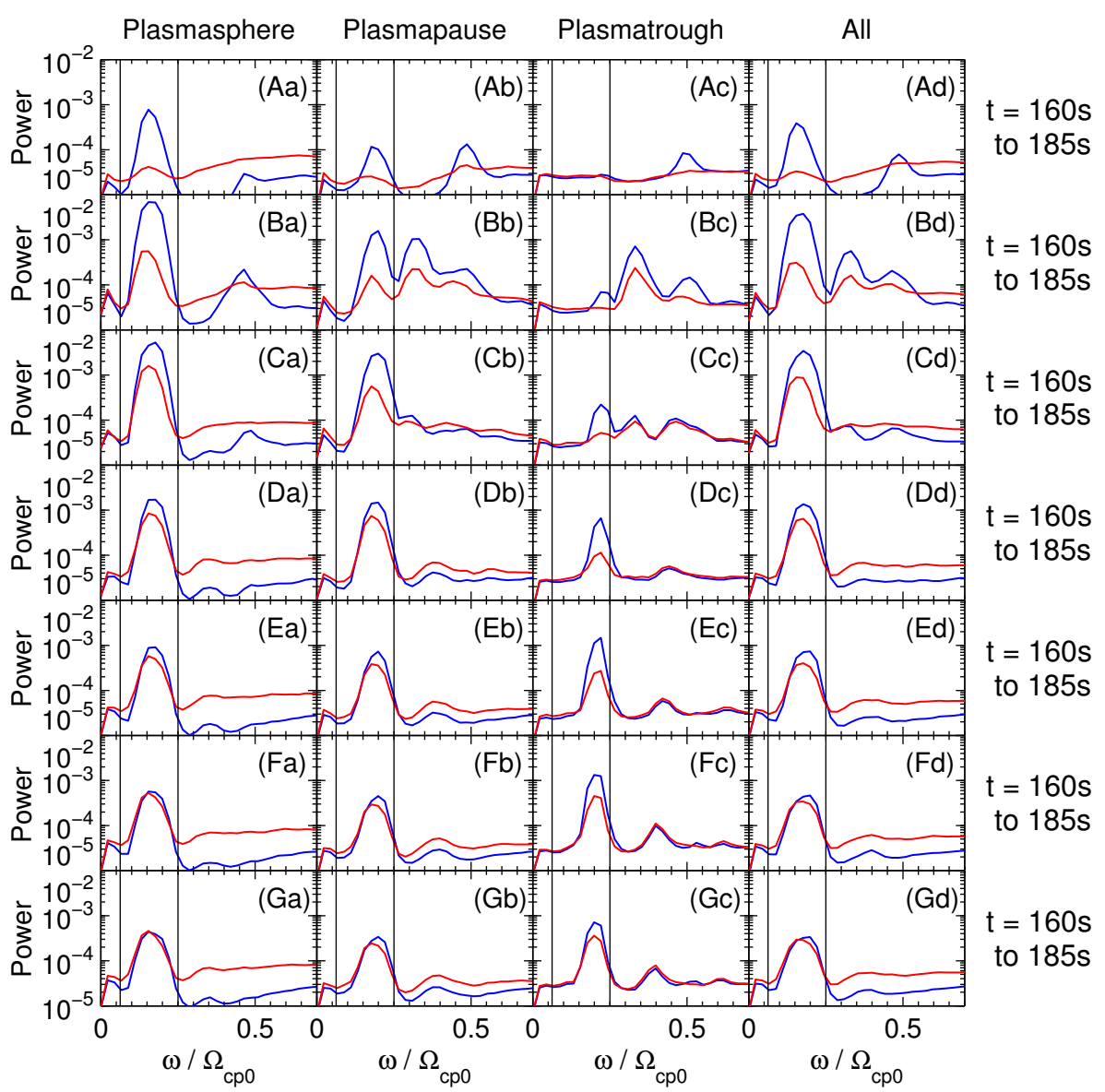
Figure 12. (a) Spectrum of normalized wave power per unit ω/Ω_{cp} observed by GOES 10 on June 9, 2001, at 2140–2150 UT at MLT = 13, and (b) spectrum from our simulation at 1900 UT at MLT = 18 with the variable composition model at $L = 5.3$ and MLAT $\sim 8^\circ$. The blue curve shows the left hand polarized wave power, while the red curve shows the right hand polarized wave power. The vertical gray lines are at the O+ gyrofrequency ($\omega/\Omega_{cp} = 1/16$) and the He+ gyrofrequency ($\omega/\Omega_{cp} = 1/4$).

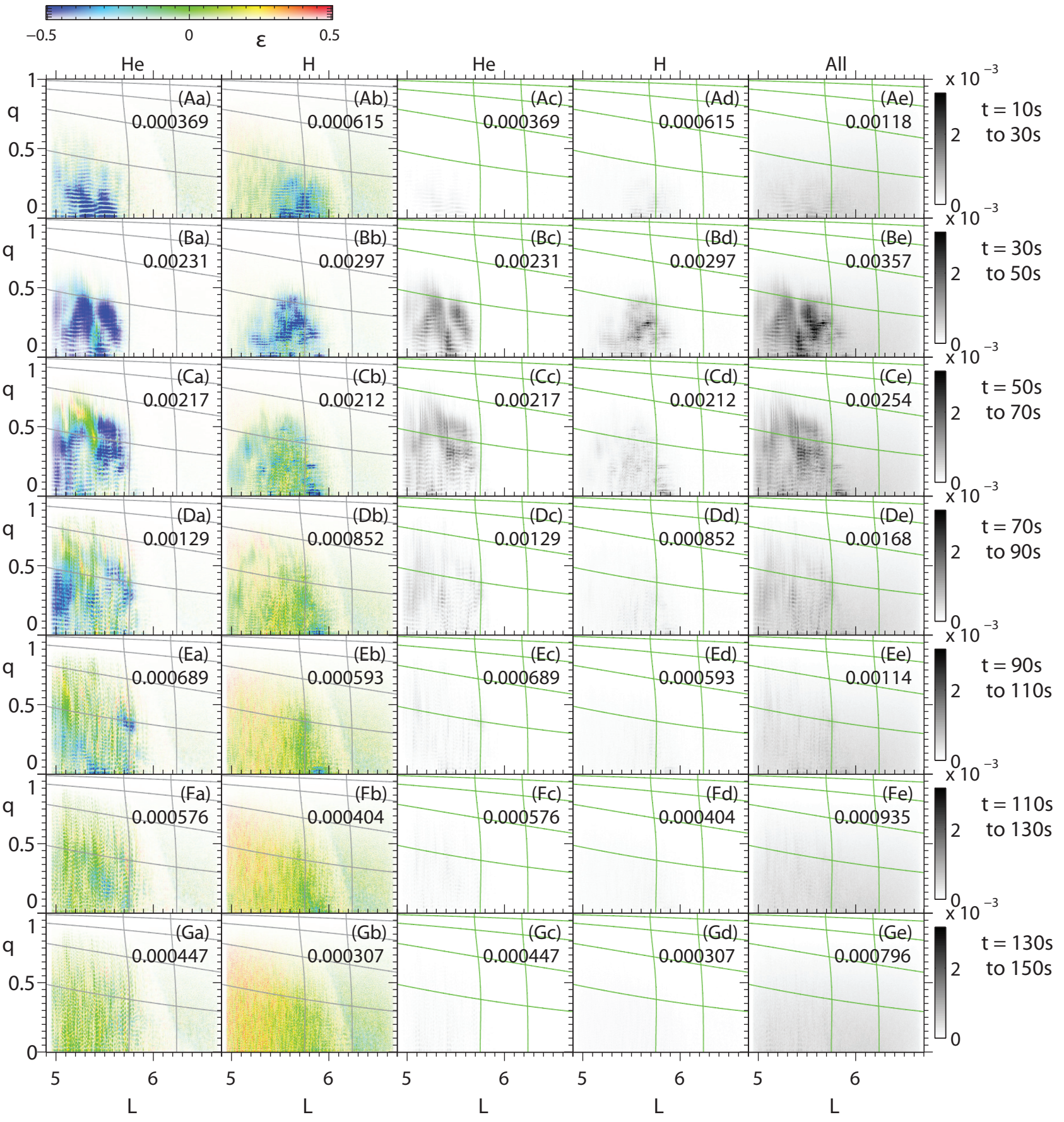
(a) $\beta_{//h}$ (b) A_h (c) $\log_{10}(n_c \text{ in cm}^{-3})$ (d) Σ_h/S_h 

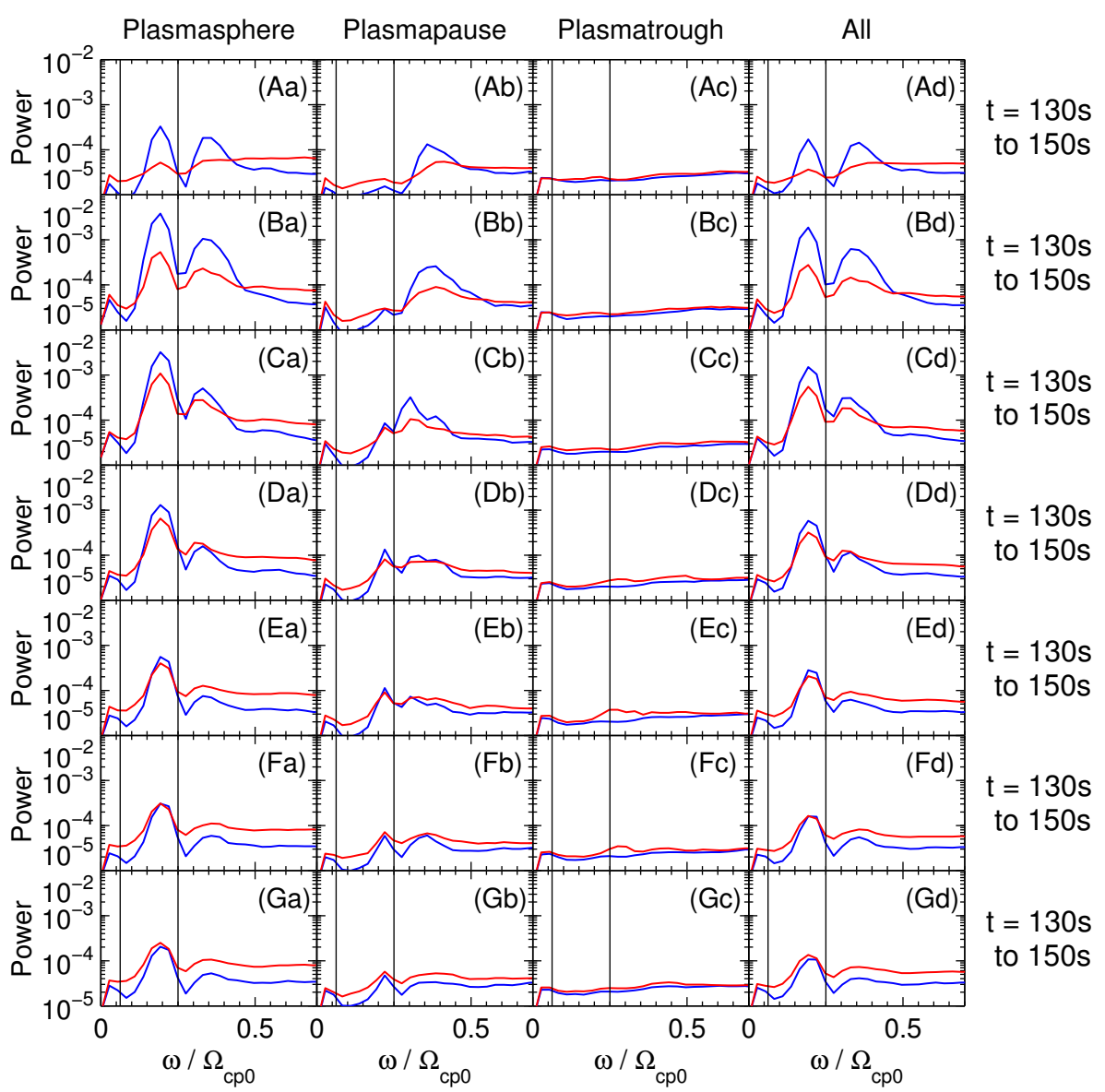


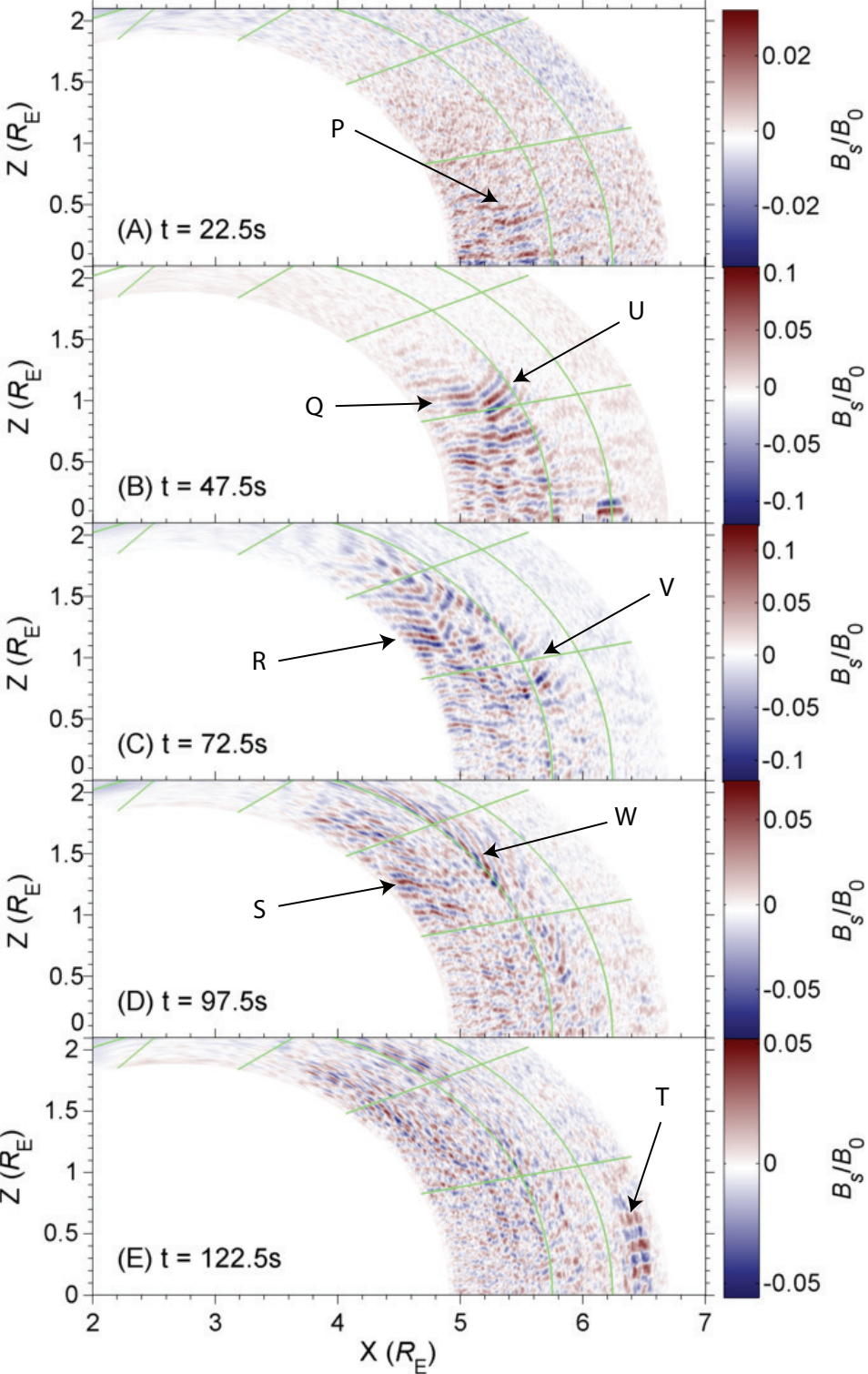












Left Hand Side of (6)

